STRUCTURAL RESTORATION AND APPLICATION OF DYNAMIC COULOMB WEDGE THEORY TO THE NANKAI TROUGH ACCRETIONARY WEDGE TOE

A THESIS SUBMITTED TO THE GRADUATE DIVISION OF THE UNIVERSITY OF HAWAI'I IN PARTIAL FULFILLMENT OF THE REQUIREMENTS FOR THE DEGREE OF

MASTER OF SCIENCE

IN

GEOLOGY AND GEOPHYSICS

MAY 2007

By
Melody A. Studer

Thesis Committee:

Greg Moore, Chairperson
Brian Taylor
Patrizia Costa Pisani

We certify that we have read this thesis and that, in our opinion, it is satisfactory in scope and quality as a thesis for the degree of Master of Science in Geology and Geophysics.

THESIS COMMITTEE

Chairperson

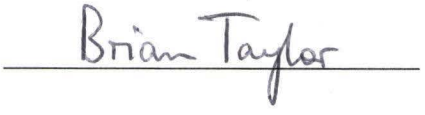

ACKNOWLEDGEMENTS

First and foremost, I would like to thank my family and friends for their support and encouragement throughout my collegiate studies. I would also like to thank my advisor, Greg Moore, whose guidance of this research made it an educational and rewarding learning experience. I wish to also express deep gratitude to Brian Taylor and Patrizia Costa Pisani whose stimulating discussions greatly benefited this research and my overall graduate experience. I would also like to specially thank Steve Martel for his influential teaching which greatly helped me in my research. I also acknowledge GeoLogic Systems for providing the University of Hawai'i with their restoration software (LithoTect®) and Bob Ratliff for his technical support.

ABSTRACT

A three-dimensional (3-D) prestack depth migrated seismic reflection data volume acquired off Shikoku Island, Japan, (Muroto Transect) images the seaward portion of the accretionary prism where the Philippine Sea plate subducts beneath the Eurasian Plate. We use structural restoration software (LithoTect®), in combination with velocity-porosity transforms derived from seismic interval velocities, to calculate and interpret total horizontal shortening lengths along four cross-sectional profiles through the volume. The results reveal that 63-82% of the total horizontal shortening results from strain. Evaluation of conjugate thrust pairs indicate a relatively low coefficient of internal friction ($\mu \approx 0.2$-0.3) and basal friction ($\mu b'' \approx 0.025$) along the wedge, suggesting that sediments deform internally yet still maintain low sediment strength during the initial stages of accretion. Application of the dynamic Coulomb theory demonstrates that the current state of the Muroto Transect outer wedge toe is in a near-critical stable state and may become critical upon small increases in either basal friction or fluid pressure observed during seismic rupture.

TABLE OF CONTENTS

LIST OF TABLES

LIST OF FIGURES

LIST OF POROSITY GRADIENTS

LIST OF CODES

CHAPTER 1. INTRODUCTION

Accretionary prisms are primary structural components of convergent margins and are described in many settings, for example, the Aleutians, Sunda, and Barbados [e.g., *Davis and von Huene*, 1987; *Kopp and Kukowski*, 2003; *Moore et al.*, 1998]. During subduction, sediment is off-scraped from the oceanic plate and accumulates in a wedge shape along the margin, constituting some of the most studied deformational features on earth. Earthquake rupture along the main basal thrust, or décollement beneath the wedge poses a large seismic and tsunami threat to numerous coastal regions worldwide. Significant progress in understanding subduction zone processes in the characterization of convergent margins during the last decade has been achieved through seismic investigation, drilling into accretionary prisms, laboratory experiments, and theoretical studies. However, understanding the mechanics and deformational response of sediments during the initial stages of accretion is limited by the lack of data constituting ambient conditions and mechanical properties of the prism.

Removing accumulated strain in the wedge through structural restoration provides horizontal shortening estimates. These estimates aid in understanding how sediment facies respond to deformation during accretion. Additionally, recent modeling advances involving critical Coulomb theory [e.g., *Davis et al.*, 1983] indicate how accretionary prisms respond specifically to the locking and rupturing behavior of the décollement throughout an earthquake cycle [*Hu and Wang,* 2006; *Wang and Hu,* 2006]. Current wedge conditions can be estimated

and better understood if one examines wedge taper, conjugate fault geometry, and horizontal shortening through structural restoration.

The Nankai Trough region is a focus for investigation partly because it has a 1300-year historical record of recurring great earthquakes, including the 1944 Tonankai (magnitude 8.1) and the 1946 Nankaido (magnitude 8.2) earthquakes [*Ando*, 1975]. Located off the southeast coast of Japan (Fig. 1), the Nankai Trough has been extensively studied in recent years during Ocean Drilling Program (ODP) Legs 131,190, and 196 [e.g., *Mikada et al.*, 2002; *Moore et al.*, 2001b, 2001c; *Taira et al.*, 1991]. Additionally, the region has been bathymetrically mapped with SeaBeam and side-scan sonar [*Ashi et al.*, 1989; *Kaiko I Research Group*, 1986], surveyed by multiple submersible and ROV dives [e.g., *Kuramoto et al.*, 2001; *LePichon et al.*, 1987a, 1987b; *Mikada et al.*, 2003], and imaged by a series of seismic reflection surveys [*Aoki et al.*, 1986, 1982; *Bangs et al.*, 1999; *Kodaira et al.*, 2000; *Leggett et al.*, 1985; *Moore et al.*, 1991; *Moore and Shipley,* 1993; *Moore et al.*, 1990, 2001a; *Nasu et al.*, 1982; *Park et al.*, 1999,2000; *Tamano et al.*, 1983]. The examination of lateral variations in outer wedge geometry along the margin is not possible with previously collected 2-D seismic data. This study examines a recent prestack depth migrated (PSDM) [*Costa Pisani et al.*, 2005] 3-D seismic reflection volume (called the Muroto Transect) originally acquired in 1999 [*Bangs et al.*, 1999; *Moore et al.,* 2001a] (Fig. 1). A schematic map view of the outer wedge study area, in addition to the orientation and location of specific profiles utilized in this study, are shown in Figure 2.

The primary goals of this paper are to estimate total horizontal shortening and to estimate current internal and basal friction parameters along the outer wedge toe of the Muroto Transect. These goals are achieved using 2-D structural restoration techniques and application of Coulomb theory to the seismic data set. The relatively small study area of this 3-D analysis provides a unique opportunity to focus on processes occurring during initial accretion, which are perhaps overlooked in studies encompassing the entire accretionary prism. Additionally, the high resolution data set allows for the examination of lateral differences in fault and overall wedge geometry.

CHAPTER 2. GEOLOGIC AND TECTONIC SETTING

The Philippine Sea Plate subducts beneath the Eurasian plate southwest of Japan at the Nankai Trough. A dense network of Global Positioning Satellites (GPS) Geodesy stations located on Japan provides a clear and detailed picture of crustal deformation along the margin (Geographical Survey Institute (GSI) of Japan). Off the coast of Shikoku Island, convergence is estimated at ~4-5 cm/yr [*Seno et al.,* 1993]. Thick hemipelagic Shikoku Basin sediments on the subducting Philippine Sea plate are partly subducted beneath and partly accreted to the toe of the margin. The partial accretion of the basin sediments, along with a high influx of turbidites, has formed the Nankai Trough accretionary prism. The subaerial Shimanto Belt located on Shikoku Island, Japan shows that the convergence and/or accretion began in the late Cretaceous [*Ohmori et al.,* 1997; *Taira et al.,* 1988; *Taira and Tashihiro,* 1987]. However, accretion was most likely not continuous throughout the history of the prism, or the wedge would be much larger than it is today [*Taira,* 2001]. The current period of accretion, estimated from drill core data, is thought to have begun during the Pliocene [*Moore et al.,* 2001c].

Previous interpretations of the Nankai Trough divide the outer wedge accretionary prism into three different tectonic zones: (1) the protothrust zone (PTZ), (2) the imbricate thrust zone (ITZ), and (3) the out-of-sequence thrust zone (OOST) [*Moore et al.*, 2001a; *Moore et al.*, 1990, 2001b] (Fig. 3). The PTZ is bounded by the deformation front in the seaward direction and the frontal thrust

landward. The ITZ begins at the frontal thrust and ends ~30 km in the landward direction and is characterized by numerous conjugate thrust faults. A large seafloor ridge at the Nankai Trough characterizes the OOST zone which extends landward from the ITZ. The inset figure of Fig. 3 shows the outer wedge toe region of the Muroto Transect, including the trench, PTZ, and first three thrust sheets of the ITZ examined in this study.

CHAPTER 3. STRUCTURAL RESTORATION

3.1 Method

Structural restoration involves modeling geologic structures in order to reconstruct the evolution of rock geometries and deformation. The assumptions of conservation of bed length or area are implemented in most existing methods for structural restoration of cross-sections. Cross-section restoration was first applied to subaerial thrust belts, using the assumption of constant bed length and thickness [*Bally et al.,* 1966; *Dalhstrom,* 1969]. The assumption of constant bed length implies that slip along bedding planes is the dominant deformation mechanism [*Davison,* 1986; *Xiao and Suppe,* 1993]. The submarine deformational environment of the Nankai Trough accretionary prism complicates the traditional bed length or area balancing assumptions [*Woodward et al.,* 1985] and, therefore, requires careful evaluation. Submarine sediment responds to accumulated strain through stratal thickening and decreased porosity. Although decreased porosity with depth is explained by uniaxial consolidation [*Taira et al.,* 1991], arcward reduction in porosity can be attributed to tectonic strains [*Bray and Karig*, 1985] and substantially contributes to shortening and convergence estimates [*Morgan et al.*, 1995].

The PSDM interval velocity model calculated by *Costa Pisani et al.,* [2005] for the Muroto Transect 3-D volume is transformed into porosity estimates using a relationship defined by *Erickson and Jarrard* [1998]. Strong correlations between corrected *in situ* shipboard porosities at drill sites 808 and 1174 (Fig.1),

and the PSDM calculated porosities allow for interpolation of sediment porosity further back in the wedge. Porosities are transformed to cross-section area ratios using a technique similar to *Morgan and Karig* [1995]:

$$\frac{A_o}{A} = \frac{(1-\gamma)}{(1-\gamma_o)} \qquad (1)$$

where γ represents the final porosity in the deformed state, and γ_0 is the initial porosity found at an undeformed reference location. The area ratio, $\frac{A_o}{A}$ describes the cross-sectional area change between the deformed and undeformed configurations.

3.2 Application to the Muroto Transect

3.2.1 Depositional Environment

Knowledge of deposition and deformation styles of the accreted sediments along the profiles provides several constraints in constructing the restorations. Unlike thick hemipelagic sediments which are deposited in the Shikoku Basin since its formation, trench sediments are transported laterally down the trench axis. The flexing of the subducting Philippine Sea plate beneath the Eurasian plate creates a depression (Nankai Trough) where turbidite deposits accumulate. They reach a maximum sediment thickness at the landward margin of the trench, and thin and onlap the hemipelagic sediments in the seaward direction. When accreted to the margin, trench sediments and Shikoku Basin sediments thicken arcward through a combination of diffuse and brittle deformational processes. The

apparent loss of the axial trench wedge facies (comprised mainly of unconsolidated muddy sand, silt turbidites, and hemipelagic mud) from the seaward portion of each thrust sheet, is mainly attributed to submarine erosion. However, periods of non-deposition of the turbidite sequence throughout the history of the wedge might also contribute to lower overall sedimentation thickness. Increased slip on faults in progressively landward thrust sheets causes an increase in seafloor relief, providing a mechanism for sediment slumping. These slumped sediments, called slope sediments, thicken in the landward direction due to the landward increase in fault slip and increased time to accumulate.

The consistent thickness of the Shikoku Basin facies within the trench (in conjunction with a constant convergence rate and sediment supply during the last 1 Myr [*Karig and Angevine,* 1985]), allows the restoration of these facies to be modeled as an approximately steady-state process. Trench sediments, however, demonstrate a slightly different depositional history. A general thickening of the outer trench wedge facies to the southwest reflects the non-uniform sedimentation associated with turbidite sequences. Implementing the restoration technique, the results reveal a slight landward increase in overall trench sediment thickness, suggesting that the accreted amount of the trench sediments has decreased through time; this would be consistent with previous studies correlating thrust fault spacing and changes in stratigraphic thicknesses [*Goff and Wiltschko,* 1992; *Karig and Angevine,* 1985].

A cross-section profile of the Muroto Transect along line 284 (Fig. 4) shows the interpretation and stratigraphic relationship between the Shikoku Basin hemipelagic facies and turbidite sequences. The décollement is located within the lower Shikoku Basin facies and separates the accreted sediment above from the subducted sediment below. Drill sites 808 and 1174, used to constrain the seismic interpretation, both penetrate the décollement and provided useful core porosity data along the base of the wedge as well as within the wedge.

3.2.2 Applied Restoration

A series of four cross-sections (lines 215, 260, 284, and 315) were interpreted and restored using the structural restoration software package LithoTect®. Restorations comprise the first, second and third thrust sheets (TS1, TS2, TS3, respectively) and the protothrust zone (PTZ-1 and PTZ-2) (Fig. 3). With the goal of removing accumulated strain from the toe of the outer wedge, an undeformed reference site is defined along crossline 685, located slightly seaward of the protothrust. Here, trench sediments reach a maximum undeformed sediment thickness. We assume the main process occurring seaward of the reference site is uniaxial compaction of sediments beneath overlying trench sediments. Compared to deformation of the accreted material due to horizontal shortening, compaction in the trench has minimal effect on the total shortening calculation. Therefore, the sediments are restored to the compaction state located at the reference site in the trench.

PSDM porosities calculated in the deformed regions are restored to the porosity calculated at the reference location using Equation 1. Porosities collected from ODP Site 808 [*Taira et al.,* 1991] provided a control section within the prism, while porosity estimates further landward in the wedge are calculated through the PSDM interval velocity data. The assumed porosities landward and at depth within the prism introduce uncertainties along the margin; however, the uses of the 3-D velocity data significantly improve upon previous limiting solutions [*Morgan et al.,* 1995].

Horizontal shortening is calculated through a length scale ratio measured along the décollement (Fig. 5). In an area balance restoration, the area within each thrust sheet remains the same as slip along the faults is restored. When applying a porosity correction to the deformed sediments within the wedge, the restored thrust sheets result in a significantly larger cross-sectional area than the original area of the deformed wedge.

Comparisons of the deformed and undeformed configurations of the four cross-sections along the Muroto Transect provide along strike estimates of horizontal shortening along the prism toe (Fig. 6). The difference in total length between the porosity-corrected and deformed states (shown in Table 1) indicates a total horizontal shortening range of about 5-6 km or about 40±2% of the initial length of ~14 km. Restoring the displaced strata based strictly on area balancing techniques recovers on average ~1-2 km of shortening.

The length difference between total horizontal shortening (which includes both a porosity loss correction and slip along faults), and a restoration that only

accounts for fault slip (area balancing) allows us to determine the component of shortening that is specifically attributed to the diffuse strain within the sediments. The results vary along the margin, ranging from a low of 63±2% at line 215 to a high of 82±2% estimated at line 315. This indicates that structural restorations applying to submarine environments, or other domains displaying volumetric strain, must account for the substantial amount of strain that affects the sediment during the initial stages of accretion.

We estimate that the total horizontal shortening results have an error of about ±2% based on the calculated interval porosity sensitivity. The error is calculated by inserting a range of initial and deformed porosities into Equation 1 based on a weighted average estimate per stratigraphic unit. The close relationships between the total shortening results reflect the similarity of accreted sediments along the entire Muroto Transect. Because the velocity model for the 3-D seismic volume is representative of rock physical properties [*Costa Pisani et al.,* 2005], the porosity model derived from the model to determine the restored area seems reasonable.

3.3 Restoration Implications

The along-trench strike distribution of horizontal shortening estimates along the Muroto Transect appears to be primarily controlled by at least two factors: (1) the amount of slip along the main thrust faults and (2) sediment response to strain accumulation throughout the wedge.

The restored sections displaying both the highest total shortening (about 40% and 42% at lines 215 and 260 respectively) and largest fault slip are located in the southwest region of the Transect (Table 1). The protothrust in the vicinity of line 215 is most distinctive in seismic section, extends furthest toward the seafloor, and displaces the most trench sediment. Toward the northeast (line 315), total shortening estimates decrease to a minimum 38% of the initial length, and the overall fault decreases too. The protothrust in this vicinity also decreases in seismic distinction, trench sediment displacement, and extends less toward the seafloor. As a result, a slightly higher amount of deformation related to slip along faults is visible toward the southwest. The general decrease in fault slip, in correlation to a smaller shortening percent toward the northeast of the survey, suggests that the main thrust faults form in the southwest portion of Nankai and propagate toward the northeast.

An additional explanation for the lateral change in fault slip is related to prism reorganization following numerous seamount subductions along the Nankai Trough. About 20 km to the northeast of the Muroto Transect, the subduction of a large ridge comprised of numerous seamounts resulted in a prominent "crescent-shaped" indention known as the Tosa Bae embayment (Fig.1). As the ridge subducted landward under the prism, the outer portion of the nearby wedge was uplifted and subsequently collapsed [*Kodaira et al.,* 2000]. If the rate of subduction is assumed to be constant throughout the history of the prism [*Karig and Angevine,* 1985], the seamounts passed under the Nankai prism about 1 million years ago. While subduction of numerous seamounts can suppress the

oceanic plate's ability to easily converge beneath the margin and inhibit slip along thrust systems, the relatively recent formation of the study area (accreted within last ~150,000 years) suggests that the previous seamount subductions are not a contributing factor of the southwest decline in fault slip. The northeast portion of the survey, located significantly closer to the Tosa Bae embayment than the southwest portion, suggests that the collapse of the prism sediments post-seamount subduction might be a contributing factor to the lower fault displacement. After the collapse, the slumped sediments quickly re-accreted to the margin. The collapse probably caused the slumped sediments to become less well-consolidated and perhaps increase overall porosity. During the initial stages of accretion, less consolidated sediment would most likely dewater rather than form brittle fractures within the wedge.

Previous horizontal shortening calculations in the vicinity of ODP Hole 808, *Morgan et al.* [1995] estimated a minimum shortening of 31% within the first two thrust sheets. The total shortening percentage attributed to accumulated strain (about 68% in the vicinity of drill site 808) was determined by a length ratio between the length of the décollement after the complete restoration and the length of the décollement after the restoration of only the folded and displaced strata (similar to the area balancing restoration in Table 1) [*Morgan et al.,* 1995]. Two possible explanations for the slightly lower calculations estimated by *Morgan et al.* [1995] include: (1) the assumption of no volume change along the base of the prism, which provides a minimum limiting solution and (2) sparse velocity logs and 2-D seismic data used in the study limit the solution for

resolving the porosity distributions. For our purposes, the PSDM velocity-porosity transforms used in this study provided increased precision in applying a porosity-correction along the prism toe.

The total amount of sediment in the deformed cross-sectional profiles (Table 1) also affects the calculated horizontal shortening estimates. The largest cross-sectional wedge area (calculated with LithoTect®) toward the southwest (lines 260 and 215 with 7.73 km^2 and 7.67 km^2 respectively) corresponds to both the largest overall horizontal shortening estimates and the largest fault slip values. The amount of area in the cross-sectional wedge is an interaction of several mechanisms, such as erosion of the axial trench wedge facies, non-uniform turbidite deposition in the trench, along strike differences in thrust fault spacing, and sediment response to deformation. Based on our interpretation of the seismic data, landward slumping and erosion of the axial trench wedge as well as relatively smaller widths in the thrust sheets toward the northeast of the volume, suggest that the change in deformed cross-sectional area along the margin may only be partially related to the accretion process.

Thrust sheet geometry along the Muroto Transect is not uniform. The deformed widths of the first three thrust sheets measured along the décollement vary between 1.27 km and 1.86 km, averaging about 1.6 km along the volume. Thrusts commonly break through at slightly different locations along accretionary prisms, thereby creating thrust sheets of different size. However, in the northeast of the volume (line 315), a secondary frontal thrust is imaged about 400 m landward of the previous frontal thrust. The "new" frontal thrust is assumed here

to be a consequence of prism collapse after seamount subduction [*Kodaira et al.*, 2000], although previous interpretations attribute the change in fault structure to the rebuilding process of the margin in order to maintain an along trench strike continuous deformation front [*Gulick et al.*, 2004]. Beyond line 315 (toward line 350), the frontal thrust imaged along the rest of the margin (lines 180-315) is no longer visible in seismic section. The ~400m landward step of the "new" frontal thrust replaces the previous frontal thrust location to the northeast. This fault re-organization provides evidence of along strike changes in overall wedge mechanics.

CHAPTER 4. APPLICATION OF COULOMB WEDGE THEORY

4.1 Method

Coulomb wedge theory is an important tool that allows estimates of current internal parameters of an accretionary prism. Low variability in surface slope and friction parameters along the margin are not readily explained with structural restoration techniques and are therefore examined through application of Coulomb wedge theory. The following sections briefly describe Coulomb theory and its application to the outer wedge toe region of the Nankai accretionary prism.

Classical Coulomb wedge theory [*Chapple*, 1978; *Davis et al.*, 1983; *Dahlen et al.*, 1984; *Dahlen*, 1984; *Zhao et al.*, 1986; *Dahlen*, 1990] is fundamental in providing an end-member understanding of critical wedge mechanics. The theory describes a solution in which the décollement slips with constant shear traction along the base of the wedge while the wedge taper remains in a critical state. Assuming a perfectly plastic Coulomb behavior in which the wedge is on the verge of shear failure everywhere, material within the wedge deforms until a critical taper is attained, analogous to a wedge of soil or snow in front of a moving bulldozer [*Davis et al.,* 1983]. After a critical taper is achieved, the wedge then slides stably over the décollement. If additional material is added at the toe, the wedge will continue to thicken and lengthen, maintaining its critical taper. Wedges with a surface slope less than critical lack the internal bulk strength

to slide on the basal thrust, and they thicken and increase their taper until slip on the basal thrust is possible.

Critically tapered Coulomb wedge solutions have been developed for many rheologies, including materials that are perfectly plastic [*Stockmal*, 1983] or viscous [*Emerman and Turcotte*, 1983] or elastic [*Yin*, 1993; *Yin and Kelty*, 2000; *Hu and Wang*, 2006]. Laboratory rock strength experiments suggest that friction and brittle failure mechanisms dominate the deformation and state of stress in the upper 10-15 km of the crust [*Hoshino et al,* 1972; *Brace and Kohlstedt*, 1980]. Therefore, Coulomb theory provides an appropriate model of accretionary wedge mechanics in the upper crust [*Davis and Engelder*, 1985].

The classical theory describes accretionary wedges over a geologic time period but does not address varying basal friction values along the wedge base during earthquake cycles. *Wang and Hu* [2006] expand the classical Coulomb theory to include basal shear traction differences between periods of interseismic locking and seismic slip. By assuming an elastic-perfectly plastic Coulomb behavior, *Wang and Hu* [2006] demonstrate how internal properties of an accretionary prism can differ between a stable regime during an interseismic period and a critical regime during a seismic event. The stress solutions of both classical and "dynamic" Coulomb theory are derived by exactly the same formulation (as shown in Figure 7), which satisfies both stable and critical wedge solutions. The maximum compressive stress σ_1 is defined by its magnitude and its orientation with respect to either the surface slope or décollement dip (ψ_o and ψ_b respectively).

The stress-strain relationship for an elastic perfectly plastic Coulomb wedge is described in detail by *Wang and Hu* [2006] and briefly summarized below. During an interseismic period, the dynamic theory assumes the outer wedge to be in a stable state. The segment of the décollement below the outer wedge may have little or no slip rate during this period [*Wang and Dixon*, 2004], and hence the basal shear stress may become extremely low. During an earthquake, when the seismogenic zone ruptures further landward along the décollement, the portion of the décollement beneath the outer wedge is forced to slip. Décollement slip would cause basal friction to become higher because it resists slip and perhaps would also cause a decrease in fault zone fluid pressure through the loss of pore water through the fault systems. If an earthquake generates enough compressive stress on the outer wedge portion of the accretionary prism, the wedge enters a critical state and shear failure occurs. When the seismogenic zone of the décollement becomes locked again, the décollement segment beneath the outer wedge is assumed to relax the earthquake generated stress within the outer wedge. Any relaxation brings a critical state wedge back to the stable elastic state.

4.2 Application to the Muroto Transect

Coulomb wedge models of accretionary prisms are based on presently observed values of wedges such as surface slope (α), basal dip (β), angle of internal friction (φ), coefficient of internal friction (μ), basal friction coefficient (μ_b), and pore-fluid pressure ratio (λ) (Fig. 7). Estimates of the wedge parameters

provide a current interseismic estimate for the Muroto Transect outer wedge toe. Given the low estimated cohesion (η) in the sediments of the outer wedge, one may reasonably apply a noncohesive model (η=0) to the study area [*Wang and Hu,* 2006; *Kopp and Kukowski,* 2003]. Four cross-sections (lines 200, 240, 280, 320) spaced 1 km apart along the Muroto Transect are examined and infer along-trench strike changes in internal and basal friction parameters that have been previously shown to affect wedge taper angles. This study also examines how an increase in basal friction and/or pore-fluid pressure ratio during a seismic event can lead to a critical state under dynamic Coulomb theory.

4.2.1 Surface Slope α and Basal Dip β

A key aspect of dynamic Coulomb theory is that the surface slope is determined by the peak basal stress achieved in large earthquakes [*Wang and Hu,* 2006]. Topographic profiles show that the Muroto Transect outer wedge toe has a nearly constant surface slope $\alpha \approx 1.5°$ with a slight increase toward the northeast $\alpha \approx 2.0°$ (Table 2). The décollement is clearly imaged by the PSDM 3-D volume and shows a steady basal dip $\beta = 1.6°$ despite the slight variations in topographic slope. The historical record of recurring great earthquakes along the Nankai Trough suggests that the average surface slope is then at least partially attributed to strain accrued during earthquake rupture.

4.2.2 Pore-Fluid Pressure Ratio λ

In existing Coulomb models, the pore-fluid pressure ratio λ is an independent variable that controls taper angle [*Davis et al.,* 1983]. According to Coulomb theory, a high λ combined with a high basal friction μ_b weakens the wedge and allows for a larger taper angle. Outer wedge geometry for numerous accretionary prisms has usually been explained by assuming near-lithostatic ($\lambda \approx 1$) values [*e.g., Dahlen,* 1990, *Lallemand et al.,* 1994]. Previous examinations of ODP Drill data for sites 808 and 1174, that penetrated the décollement within the Muroto Transect suggest inhibited dewatering and overpressure development seaward of the frontal thrust [*Screaton et al.,* 2002]. The overpressure estimates suggest that the lower hemipelagic sediments have insufficient permeability for fluid escape because of the rapid loading of the turbidite sequences within the trench. However, recent fluid pressure monitoring within site 808 does not support the current presence of high pore-fluid pressures along the Nankai subduction zone [*Davis et al.,* 2006]. Additionally, *Wang and Hu* [2006] demonstrate that high overpressures within the wedge are not required during an interseismic period but may be reached during an earthquake. Realistically, pore-fluid pressures reflect the combined influence of numerous parameters, such as sediment permeability, plate-convergence rate, fluid migration through faults, and the thickness and stratigraphy of incoming sediments [*Saffer and Bekins,* 2002]. Numerical models of hydrologic controls of accretionary prisms based on the estimated plate-convergence rate and accreted sediment permeability of the

Nankai accretionary prism estimate a lower, more moderate $\lambda \approx 0.5$ [*Saffer and Bekins,* 2002].

4.2.3 Internal and Basal Friction Coefficient μ and μ_b"

The geometry of the frontal conjugate thrust faults along the outer wedge toe provides a mechanism to estimate the internal friction coefficient μ (Fig. 8). The observed faults are assumed to represent fresh Coulomb fractures that are not significantly rotated [*Gutscher,* 1996, *Kopp and Kukowski,* 2003]. The Coulomb failure criterion is satisfied along two planes inclined at an angle of $45°-\frac{\phi}{2}$ to the σ_1 axis. If the thrusts are assumed to form along preferred slip lines, it is possible to calculate the orientation of the maximum compressional stress σ_1. Through mathematical relations previously described by *Davis and von Huene* [1987] and *Kopp and Kukowski* [2003], values of μ, φ, ψ_o, ψ_b, are determined based on the observed dip angles of conjugate thrust faults, δ_b and δ_f. Frontal and back fault dips are related to the surface slope and décollement dip ($\delta_{b\text{-REL}}$ and $\delta_{f\text{-REL}}$ respectively) through simple geometric relations [*Kopp and Kukowski,* 2003] (Table 2). Principal stress orientations for the current wedge are shown in Fig. 8 with blue arrows, with the larger of the two representing the maximum compressive stress σ_1. During an earthquake, the σ_1 stress orientation relative to the surface ψ_o decreases based on a linear elastic model until a critical angle is achieved as a consequence of increased basal friction and pore-fluid pressure [*Wang and Hu,* 2006].

Previous studies along the Nankai margin have assumed high internal friction values for the wedge such as μ=0.85 [*Saffer and Bekins*, 2002]. However, such high values are appropriate for crystalline or well-consolidated sedimentary rocks which are not characteristic of the Nankai outer wedge toe. Estimates of internal friction varying from μ=0.3-0.5 have been previously calculated from conjugate thrust faults along the Nankai (Kii Peninsula) and Cascadia margins and are appropriate for soft accreting sediments [*Wang and He,* 1999]. Within the Muroto Transect, *Feeser et al.* [1993] has calculated estimates of the angle of internal friction (φ = 24.4°) from micro-structures at ODP Hole 808c, which yields a μ=0.45 (μ= tan(φ)) [e.g., *Davis et al.,* 1983; *Dahlen et al.,* 1984; *Zhao et al.,* 1986]. However, Coulomb wedge theory describes failure slip planes across the entire wedge, and is better modeled using the main thrust fault geometry.

Wang and Hu [2006] describe a basal friction property μ_b'' that depends on both the intrinsic basal friction coefficient μ_b and the effect of the pore-fluid pressure ratio λ within the wedge. In relation to the classical Coulomb theory, $\mu_b''=\mu_b(1-\lambda)$. *Wang and He* [1999] determined the present μ_b'' value to be around 0.03-0.05 for the Nankai subduction zone off the Kii Peninsula. Based on the calculations of μ and ψ_o in this study, and assuming a reasonable value of λ = 0.5, an observed basal friction property μ_b'' (Table 3) ranging from $\mu_b'' \approx$ 0.02-0.03 is calculated for the current state of the outer wedge toe along the Muroto Transect.

4.2.4 Sediment Strength

Knowledge of the strength of sediments is crucial to understanding subduction zone mechanics because sediment strength controls (1) the state of stress at which deformation takes place, (2) the coupling between the converging lithospheric plates, and (3) the distribution of stress in the overlying plate [*Davis and von Huene,* 1987]. Sediment strength is calculated through the ratio between the effective basal friction μ_{beff} derived by *Kukowski et al.* [2001] and the coefficient of internal friction μ (Table 3). The ratio $\frac{\mu}{\mu_{beff}}$ expresses the strength ratio between the wedge and the décollement, as discussed by *Davis and von Huene* [1987] and *Kukowski et al.* [2001]. The results for μ ranging from about 0.2-0.3 and the angle of the principle stress direction with the décollement ψ_b ranging from about 7°-11° from this study indicate that the accreted sedimentary sequence is about 2.6±0.5 times stronger than the detachment zone.

Sediment strength can be affected by the loss of pore fluids through fault systems. Near the wedge toe, pore fluids can be expelled through the trench turbidite facies where numerous fractures act as conduits. Dewatering is highly effective across stratigraphically controlled boundaries in the presence of fluid migration paths [*von Huene and Klaeschen,* 1999]. While the hemipelagic Shikoku Basin facies are less able to easily dewater due to the high influx of overlying trench turbidites, the likelihood is that dewatering along the main thrust faults at least partially contributes to wedge strength within the toe.

Other accretionary prisms, such as the Sunda and Aleutian margins, have estimated sediment strength 2.3 and 1.5 times stronger than the basal detachment respectively [*Kopp and Kukowski,* 2003; *Davis and von Huene,* 1987]. The strength ratio suggests that either weak material in the wedge, overpressuring near the décollement, or a combination of both, is a common scenario in numerous accretionary prisms. The slightly higher strength ratio estimated within the outer wedge toe along the Nankai margin suggests either higher overpressure along the décollement and/or weaker wedge material compared to the entire accretionary prism.

4.2.5 Coulomb Wedge Modeling

The α-β plot in Figure 9 shows five pairs of critical α and β values for an estimated value of λ=0.5. The lower solid lines are for a compressively critical (on the verge of compressive failure) state, and the upper dashed lines represent the extensionally critical (on the verge of gravitational collapse) state. The lines bracket a stable region characteristic of an interseismic period during an earthquake cycle. Four of the five critical state trajectory pairs utilize calculated values of μ and μ_b'' determined from the frontal conjugate thrust faults along the Muroto Transect. For comparison to our estimates of the outer wedge toe, critical curves of a previous estimate of μ=0.7 and μ_b''=0.04 [*Wang and Hu,* 2006] representative of the entire Nankai accretionary prism including both inner and outer wedges are also shown in Figure 9. For the purposes of this study, a relatively high internal friction coefficient may not be representative of the outer

wedge toe; however, we include the higher value for discussion purposes. If we model the outer wedge toe using μ=0.7, μ_b''=0.04 and λ=0.5, the observed taper angles measured along the profiles maintain would still reflect a stable state, but would require a greater increase in basal friction to reach a critically compressed state during an earthquake.

All of the current wedge geometries in Figure 9 lie within their respective stable state regimes but are relatively close to the compressively critical states. For a wedge of higher internal strength μ, a larger increase in basal friction μ_b'' along the décollement would need to be achieved during an earthquake for the wedge to be considered compressively critical.

A key aspect of dynamic Coulomb theory is that higher basal friction can be achieved during great earthquakes. *Wang and Hu* [2006] demonstrate in detail how principal stress orientations in an elastic-perfectly plastic Coulomb wedge are affected by basal friction. According to the theory, a large enough increase in basal friction causes ψ_o to decrease until it reaches a critical angle. *Wang and Hu* [2006] refer to the change of ψ_o with respect to μ_b'' as the elastic stress path. Figure 10 shows the elastic stress path for two specific profiles (lines 320 and 200) which display the largest difference in surface slope and internal friction coefficient of the four profiles. For each geometry, ψ_o changes between its two critical values (compressive and extensional) corresponding to the two critical μ_b'' values. When $\psi_o = 45°$, the value of μ_b'' is considered to be the value of a wedge in a neutral stable state. The current (interseismic) estimations of μ_b'' and ψ_o along the cross-sectional profiles are indicated by a star.

According to dynamic Coulomb theory, the pore-fluid pressure ratio λ within the wedge must also increase during coseismic compression. Therefore, stress within the wedge should move to a stress path for a higher λ value during an earthquake. After the earthquake, the stress path should move to a lower λ value because of fluid drainage along the faults and stress relaxation. As seen in Figure 10, the critical values of μ_b'' decrease as λ increases. For discussion purposes, we propose a value of λ=0.8 in the outer wedge toe during a seismic event. In this scenario, the fluid pressure increase alone would push the current outer wedge toe into a critical state on the verge of compressive failure. For a wedge of μ=0.45 [*Feeser et al.,* 1993], an increase of λ to 0.8 in addition to an increase in μ_b'' of about 0.006 would cause critical compression. A stronger wedge of μ=0.7 [*Wang and Hu,* 2006] and λ=0.8 would require a 0.02 increase in μ_b'' to achieve a compressively critical state. If the Muroto Transect is in a current stable state (with $\mu \approx 0.2$), the result of this study suggests that the pore-fluid pressure ratio λ along the décollement is less than 0.8 but likely greater than 0.5. This suggests that a slight increase in the pore-fluid pressure ratio and/or basal friction would cause compressive failure in the outer wedge toe of the Muroto Transect regardless of slight variations in intrinsic wedge strength. A key observation of our results relies on the implication that the Muroto Transect outer wedge toe is currently in a near-critical state.

4.3 Coulomb Wedge Implications

Low variability in surface slope appears to be controlled by two main factors: (1) small along trench-strike lateral variations in basal friction and (2) the internal friction coefficient μ. Differences of the surface slope along the entire Nankai accretionary wedge has been previously attributed to fluctuations in basal friction [*Moore et al.,* 1990]. On a much smaller scale, the results along the Muroto Transect indicate that higher basal friction increases with surface slope. This suggests that slight variations (±0.01) in basal friction μ_b''may partially control surface slope topography. Additionally, along-trench strike variations in sediment strength μ along the Muroto Transect play an important role in the evolution of the structural characteristics of the subduction zone. The model results suggest that an increase in μ decreases critical taper, which agrees with overall Coulomb wedge mechanics.

Basal friction μ_b'' values calculated from the observed frontal conjugate fault pairs along the margin as well as critical values of μ_b'' are shown in Table 3. The results indicate that an average increase of about 0.003 to the reference values of μ_b'' will cause a compressively critical state along the outer wedge toe if λ remains constant at 0.5. Interestingly, if the internal friction coefficient is slightly higher (μ=0.45), as described by *Feeser et al.,* [1993], a greater increase of ~0.03 in μ_b'' would cause the wedge to become critical. Furthermore, if μ=0.7 [*Wang and Hu,* 2006], μ_b'' would need to increase by an average of 0.07 to make the wedge critical. Thus, the results suggest that higher basal friction is needed for critical deformations in a wedge with higher intrinsic wedge strength. This study

demonstrates that the Muroto Transect is currently significantly closer to a critical state than previously modeled. This implication is supported by recent data from *Ito and Obara* [2006] which reported transient clusters of very low frequency earthquakes along the Nankai coast over the past few years. This indicates that parts of the outer wedge are possibly in a near-critical stable state so that failure can occur upon a small perturbation of basal friction μ_b''.

CHAPTER 5. STRUCTURAL RESTORATION AND COULOMB WEDGE SYNTHESIS

Relations between results from our structural restoration and application of Coulomb wedge theory allow for further implications along the toe of the Muroto Transect. The inferred current near-critical state of the outer wedge toe represents a time-dependent accumulation of strain. Horizontal shortening estimates in addition to current estimates of internal and basal friction parameters within the toe provide constraints on how the current outer wedge toe has been deformed.

5.1 Implications along the Northeast portion of the Muroto Transect

Compared to the southwest section of the Muroto Transect, the northeast section has relatively higher taper angles and basal friction estimates which correspond to a smaller recovered total shortening and overall fault displacement (Fig. 11). Basal friction contributes directly to the observed taper; however, these small-scale fluctuations do not seem to be a contributing factor of overall fault displacement within the wedge. While higher basal friction resists slip along the décollement and supports a larger taper angle, the slip on faults within the wedge remains low.

Compared to the rest of the seismic volume, relatively low percentages of horizontal shortening are estimated in this area (~38±2% of the initial length of ~14 km). While smaller amounts of slip on faults in the wedge are the main

contributor to the smaller restoration length, the Coulomb analysis suggests that the coefficient of internal friction in the northeast ($\mu \approx 0.2 \pm 0.02$) represents slightly weaker sediment that possibly has a slightly higher pore fluid space. Thus, the sediment would preferentially deform (dewater) before yielding large brittle slip along faults. A lower coefficient of internal friction μ in conjunction with lower fault slip suggests that during the initial stages of accretion, sediments preferentially deform most likely through drainage of pore fluid through fault systems.

5.2 Implications along the Southwest portion of the Muroto Transect

The southwest section of the Muroto Transect estimates of taper angles and basal friction associate with slightly higher shortening percentages and sediment strength ($\mu \approx 0.3 \pm 0.02$). Relatively higher fault slip in this region has an inverse relationship with the contribution of strain deformation estimated from the structural restorations. A relatively high percentage of the total horizontal shortening attributed to strain (~82±2% at line 320) corresponds to a region with the least fault slip and overall wedge strength μ. While these correlations seem counterintuitive, the increased strain can be explained by the fact that smaller slip along the faults have a decreased length of individual deformed reflectors within the thrust sheets and, hence, recover a shorter undeformed restored state. For example, in the area balance restorations, a much shorter length is recovered along line 315 (9.55 km) than line 215 (10.54 km). The restored length difference

between the northeast and southwest portions of the survey of about 1 km contributes substantially to the relative percentage attributed to internal strain.

The low estimate of basal friction found at line 200 ($\mu_b'' \approx 0.02 \pm 0.01$) and relatively stronger wedge ($\mu \approx 0.3 \pm 0.02$) are the main contributing factors in the overall low wedge taper. To create a compressively critical wedge, this region would require a relatively higher increase in basal friction (or decrease in μ) compared to the northeast section of the survey. Therefore, the southwest region of the survey is currently in a more stable state compared to the northeast region (as seen in Figure 9).

The relatively more stable wedge is reflected by the difference in backthrust geometry along the margin. While the frontal thrust geometry is relatively constant along the entire prism, backthrusts in the southwest are not as steeply dipping as the backthrusts in the northeast. The larger angle between the frontal and backthrust fault pair in the southwest allows for a relatively larger angle of internal friction φ, coefficient of internal friction μ, and lower stress orientation angle ψ_o in the southwest of the survey as compared to the northeastern part of the study area.

CHAPTER 6. CONCLUSIONS

The analysis of the Muroto Transect outer wedge toe focused on structural restoration and application of dynamic Coulomb wedge theory. Our results reveal about 63±2% in the northeast to about 82±2% in the southwest of total shortening of ~5.5 km is due to accumulated strain within the sediments of the Nankai outer wedge toe. Along strike shifts in the contribution of strain are attributed to changes in fault slip and sediment dewatering during accretion. Our results indicate that a significant amount of deformation occurs within sediments during the initial stages of accretion, creating a total horizontal shortening of ~40±2% within the first three thrust sheets of the wedge.

The geometry of the frontal conjugate thrust faults imply the coefficient of internal friction $\mu \approx 0.3 \pm 0.02$ for sediments in the southwest and $\mu \approx 0.2 \pm 0.02$ for sediments in the northeast part of the survey. Collapse of the prism after a large ridge subducted to the northeast of the Muroto Transect may contribute to a change in fault geometry in the vicinity of lines 315-350. Additionally, possible propagation of the main thrust faults along the margin from the southwest to northeast provide a mechanism for relatively smaller amount of fault slip toward the northeast of the volume. Estimates of basal friction ($\mu_b'' \approx 0.03 \pm 0.01$) along the entire Muroto volume are reflective of the current interseismic period of the Nankai accretionary prism. A gradual increase in surface slope along the margin is attributed to an increases in basal friction. The outer wedge toe is in a near-

critical stable state and may become critical upon small increases in either basal friction, pore-fluid pressure, or both.

APPENDIX A: Tables

Table Captions

Table 1:

Horizontal shortening estimates of four seismic profiles along the Muroto Transect

Table 2:

Observed step-up angles and inferred principal stress orientations along four seismic profiles along the Muroto Transect

Table 3:

Calculated basal friction and strength ratio properties along four seismic profiles along the Muroto Transect

Transect	Deformed Length	Area Balance Restored Length	Porosity Corrected Restored Length	Area Balance Shortening (%)	Porosity Corrected Shortening (%)
215 *(Deformed Area = 7.67 km^2)*					
total	8.45	10.54	14.1	19.8	40.1
TS3	1.84	2.94	4.63	37.4	60.2
TS2	1.36	1.80	2.80	24.4	51.4
TS1	1.74	2.19	2.66	20.5	34.6
PTZ-1	1.91	1.98	2.23	3.50	14.3
PTZ-2	1.59	1.60	1.78	0.60	10.7
260 *(Deformed Area = 7.73 km^2)*					
total	8.59	10.05	14.89	14.5	42.3
TS3	1.58	2.00	3.40	21.0	53.5
TS2	1.48	2.10	2.64	29.4	51.9
TS1	1.70	1.98	2.56	13.9	45.6
PTZ-1	2.19	2.37	3.03	7.5	34.6
PTZ-2	1.53	1.58	2.07	3.2	19.1
284 *(Deformed Area = 7.47km^2)*					
total	8.35	9.70	13.85	13.9	39.7
TS3	1.86	2.38	3.43	22.0	45.7
TS2	1.27	1.61	2.64	21.2	51.9
TS1	1.44	1.69	2.56	15.1	44.0
PTZ-1	2.10	2.29	3.03	8.4	30.8
PTZ-2	1.69	1.70	2.07	0.3	18.1
315 *(Deformed Area = 7.40 km^2)*					
total	8.62	9.55	13.9	9.8	37.9
TS3	1.36	1.62	2.18	16.7	37.8
TS2	1.78	2.38	3.13	24.9	43.1
TS1	1.79/1.0*	1.87/1.08*	2.84/1.67*	4.3/7.4*	36.9/40.1*
PTZ-1	2.13	2.18	2.38	2.2	10.5
PTZ-2	1.54	1.57	1.70	1.9	9.4

*A secondary frontal thrust is visible at line 315 as previously described by *Gulick et al.,* [2004]. The first number corresponds to the frontal thrust extending from the southwest to northeast along lines 190~320. The second number corresponds to the landward stepping frontal thrust imaged between lines ~320-350.

Table 1

Table 2

Line	α ($\pm 0.5°$)	β ($\pm 0.5°$)	$\delta_{b\text{-}REL}$ ($\pm 1°$)	$\delta_{f\text{-}REL}$ ($\pm 1°$)	φ ($\pm 1°$)	μ (± 0.02)	ψ_b ($\pm 1°$)	ψ_o ($\pm 1°$)
200	1.4	1.6	46.6	28.4	15	0.27	9.1	6.1
240	1.5	1.6	45.6	31.4	13	0.23	7.1	4.0
280	1.6	1.6	49.6	28.4	12	0.22	10.6	6.9
320	2.0	1.6	50.6	29.4	10	0.18	10.6	7.0

Table 3

Line	μ_b'' (observed) (±0.01)	μ_b'' (compressively critical) (±0.01)	μ_b'' (neutral) (±0.01)	μ_b'' (extensionally critical) (±0.01)	$\mu_{b\text{-eff}}$ (±0.02)	$\frac{\mu}{\mu_{b\text{-eff}}}$ (strength ratio) (±0.5)
200	0.021	0.033	0.014	0.004	0.107	2.52
240	0.027	0.031	0.015	0.006	0.071	3.26
280	0.024	0.032	0.016	0.007	0.093	2.36
320	0.030	0.033	0.020	0.011	0.075	2.40

*$\lambda = 0.5$, μ = calculated value from Table 2

APPENDIX B: Figures

Figure Captions

Figure 1:

(Right) Regional Tectonic map of Japan showing setting of the Nankai Trough study area (red box). (Left) Shaded relief map of the Nankai Trough, with locations of ODP drill sites (808, 1174, 1173) used in this study, the Muroto Transect seismic reflection volume (yellow) and the outer toe region of the Muroto Transect (red box). Convergence rate is estimated at 4-5 cm/yr at an azimuth ~305° [*Seno et al.,* 1993; *Gulick et al.,* 2004]. (modified from *Shipboard Scientific Party*, [2001]).

Figure 2:

Map view of the study region of the Muroto Transect. The distribution of restored lines (215, 260, 284, 315) and lines analyzed with Coulomb wedge theory (200, 240, 280, 320) are shown along the volume. Arrows represent the orientation of the seismic survey. The reference location along crossline 685 used in the structural restoration is shown. The study area comprises crossline 400 to about 1100. Broken line segments represent a break in the profile segment.

Figure 3:

Schematic profile of the Nankai accretionary prism showing the location of the outer wedge and different tectonic zones. The outer wedge toe region, comprising

the first, second, and third thrust sheets (TS1, TS2, and TS3 respectively) and protothrust region (PTZ-1 and PTZ-2), used in our structural restoration are shown in the magnified subset. Seaward of the reference location, tectonically undeformed trench sediments reach a maximum sediment thickness. Landward of the reference site (in the PTZ-2 region), small-scale backthrusts begin to thicken and deform the sediment pile.

Figure 4:

Seismic cross-section profile and interpretation of Line 284 within the Muroto Transect. Drill sites 808 and 1174 are shown in their respective locations and are used to constrain the interpretation. The stratigraphic column defines the individual sediment facies. The décollement (dashed line) forms within the Lower Shikoku Basin facies and separates the accreted material (above) from the subducted material (below).

Figure 5:

Schematic illustration of the horizontal shortening calculation used in this study. Lengths are measured from the reference location (crossline 685) to the end of the third thrust sheet along the décollement. An area balance restoration corrects for fault slip along the main thrust faults, but maintains the same area within the thrust sheets (A1, A2, A3, A4). Application of a porosity correction to the deformed sediments yield a larger restored cross-sectional area and restored

length (A1 + porosity area, etc.). Total horizontal shortening is a ratio between the difference in length ($L_i - L_f$) and the restored length (L_f).

Figure 6:

Interpreted PSDM profiles and corresponding porosity-corrected structural restorations across the Muroto Transect region of the Nankai Trough shown at 2:1 vertical exaggeration. Main stratigraphic facies correlated within the protothrust zone, first, second, and third thrust sheets are shown in their defined colors. Trench fill sediments are orange and yellow, facies transition is green, and the Shikoku Basin sediments are blue and purple. The locations of ODP Hole 808 and 1174 are also indicated along line 284. Restored sediment thicknesses represent the compaction state found at the reference location (Crossline 685). The apparent loss of the outer trench wedge facies in the thrust sheets is attributed to submarine erosion. Restored estimates of the eroded surface, and slope sediment facies are shown with dashed lines.

Figure 7:

Cartoon illustration of a critical or stable wedge coordinate system (x,z) based on a similar figure by *Wang and Hu,* [2006]. Parameters include maximum compressive principal stress σ_1, surface slope α, basal dip β, water depth D, basal tractions and principal stress orientation angles ψ_o and ψ_b.

Figure 8:

Detailed views of the frontal thrust region along the Muroto Transect shown at 1:1 vertical exaggeration. The structural analysis of the Nankai accretionary wedge is based on the geometry of the conjugate pair of forethrust and backthrust faults imaged in the PSDM profiles. The dip angles of the thrusts δ_f and δ_b are measured from the horizontal and are used to calculate the principal stress orientations (blue arrows) through equations presented by *Kopp and Kukowski* [2003]. The larger of the stress orientations represents the larger principal stress σ_1.

Figure 9:

Surface slope angle versus basal dip based on noncohesive Coulomb wedge theory. Dashed and solid lines represent the extensionally and compressively critical states respectively for the shown set of material parameters. The critical states bracket a stable region for the wedge. The outer-wedge toe geometry variations for the profiles along the Muroto Transect are shown with colored dots correlating to their respective critical taper trajectories. The critical state for a relatively stronger wedge (μ=0.7, and μ_b''=0.04) as used by *Wang and Hu,* [2006] are also shown for comparison.

Figure 10:

Elastic stress paths for profiles 320 and 200 along the Muroto Transect assuming internal wedge parameters calculated from frontal thrust geometries. Black stars

indicate the current state of the wedge. The inset shows the critical values of basal μ_b'' as a function of pore fluid pressure ratio λ for the calculated value of internal friction μ and 0.45. All cases assume a noncohesive wedge ($\eta = 0$).

Figure 11:

Summary of estimated trends: surface slope α, internal friction μ, basal friction μ_b'', and percent of shortening attributed to strain along the Muroto Transect outer wedge toe. Red arrows point toward increasing values.

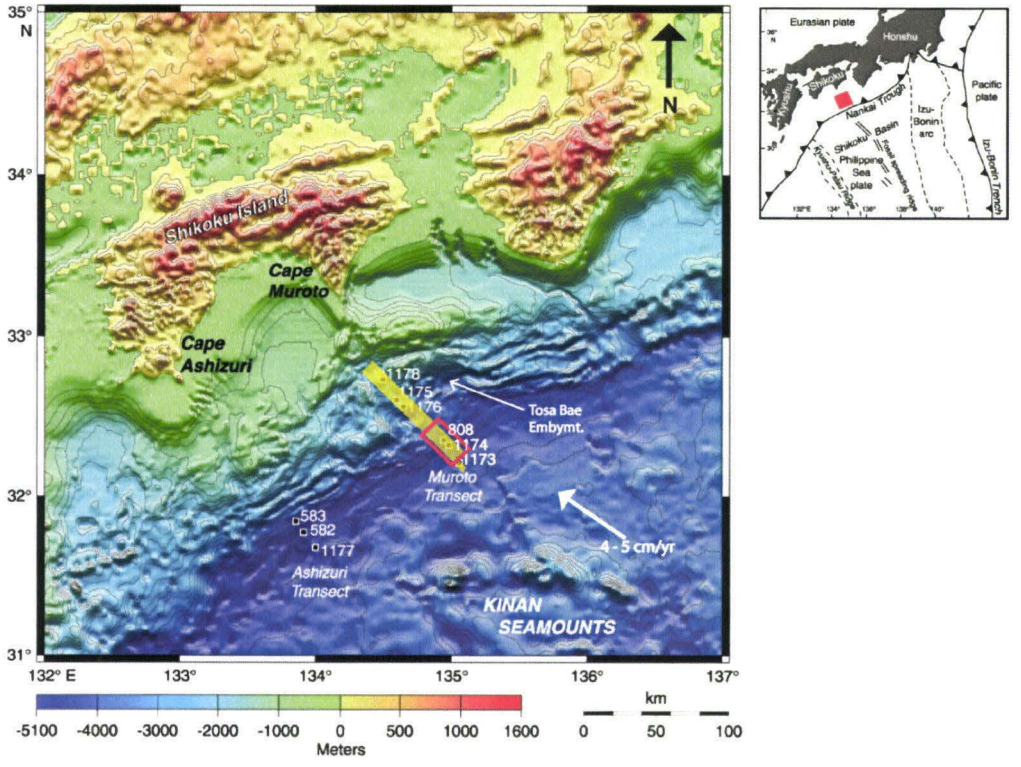
35° N
34°
33°
32°
31°
132° E
133°
134°
135°
136°
137°
N
Shikoku Island
Cape Muroto
Cape Ashizuri
1178
1175
1176
808
1174
1173
Tosa Bae Embymt.
Muroto Transect
583
582
1177
Ashizuri Transect
4 - 5 cm/yr
KINAN SEAMOUNTS
-5100 -4000 -3000 -2000 -1000 0 500 1000 1600
Meters
km
0 50 100
Eurasian plate
Honshu
Shikoku
Nankai Trough
Pacific plate
Izu-Bonin arc
Shikoku Basin
Philippine Sea plate
Izu-Bonin Trench

Figure 1

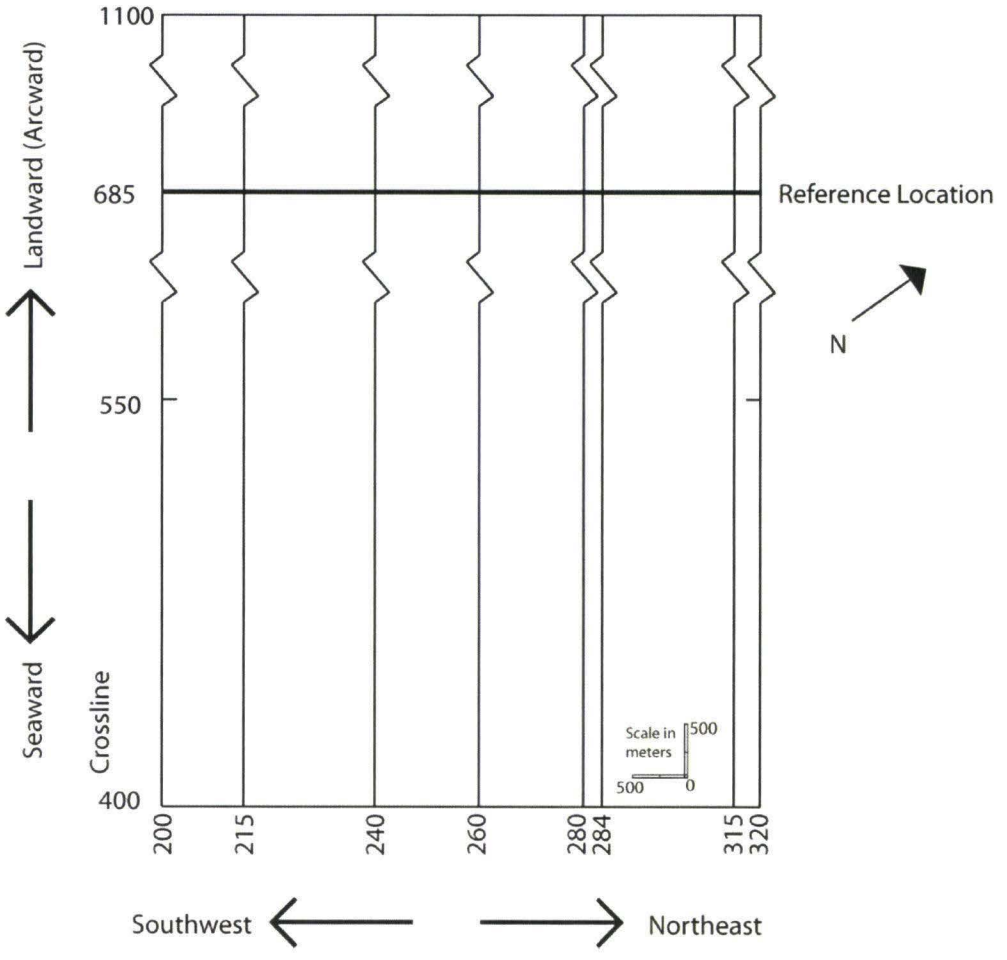
1100
685
550
400
Landward (Arcward)
Seaward
Crossline
Reference Location
N
Scale in meters
500
500
0
200
215
240
260
280
284
315
320
Southwest
Northeast

Figure 2

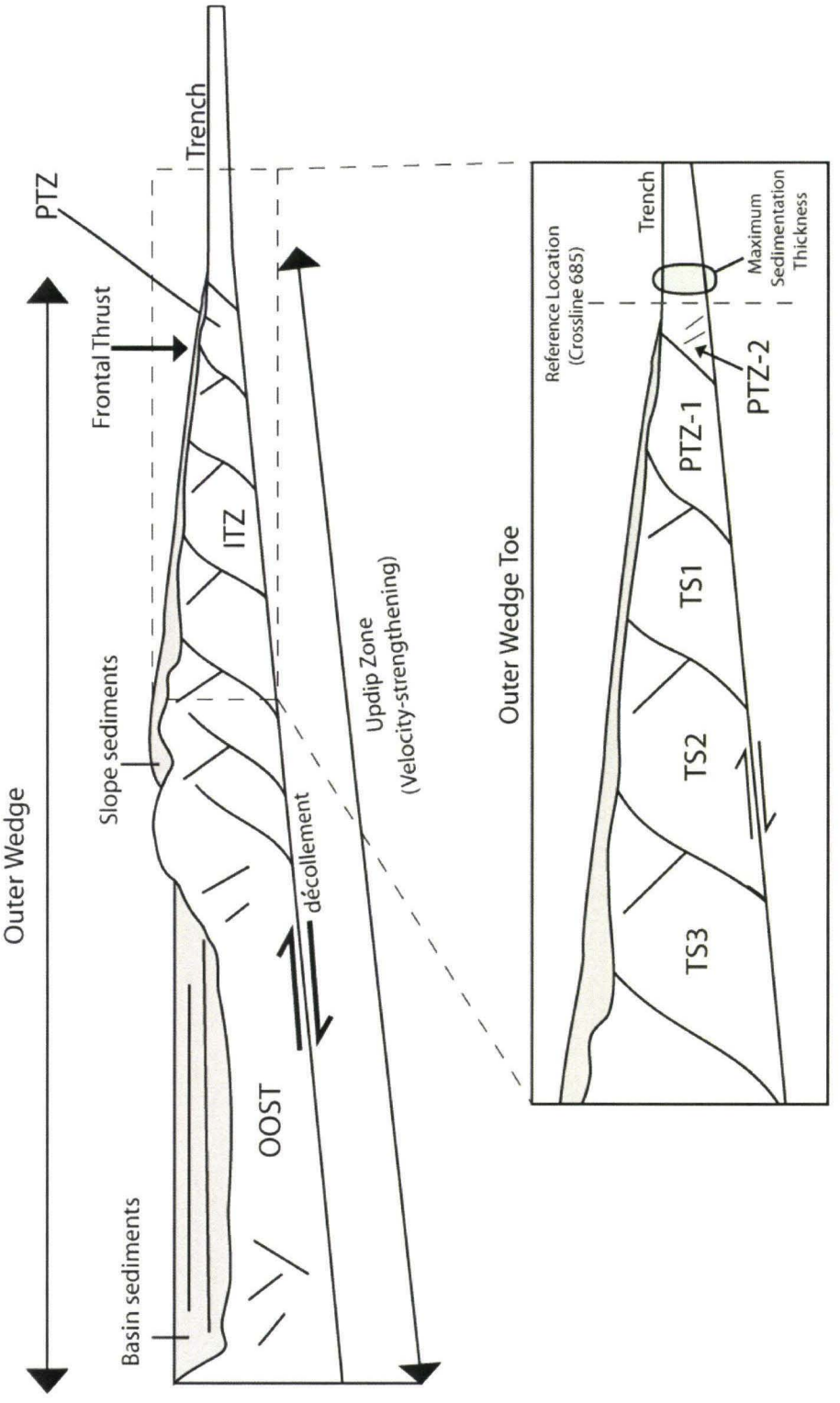
Trench
PTZ
Frontal Thrust
ITZ
Slope sediments
Outer Wedge
Basin sediments
OOST
décollement
Updip Zone
(Velocity-strengthening)
Outer Wedge Toe
Reference Location
(Crossline 685)
Trench
Maximum
Sedimentation
Thickness
PTZ-2
PTZ-1
TS1
TS2
TS3

Figure 3

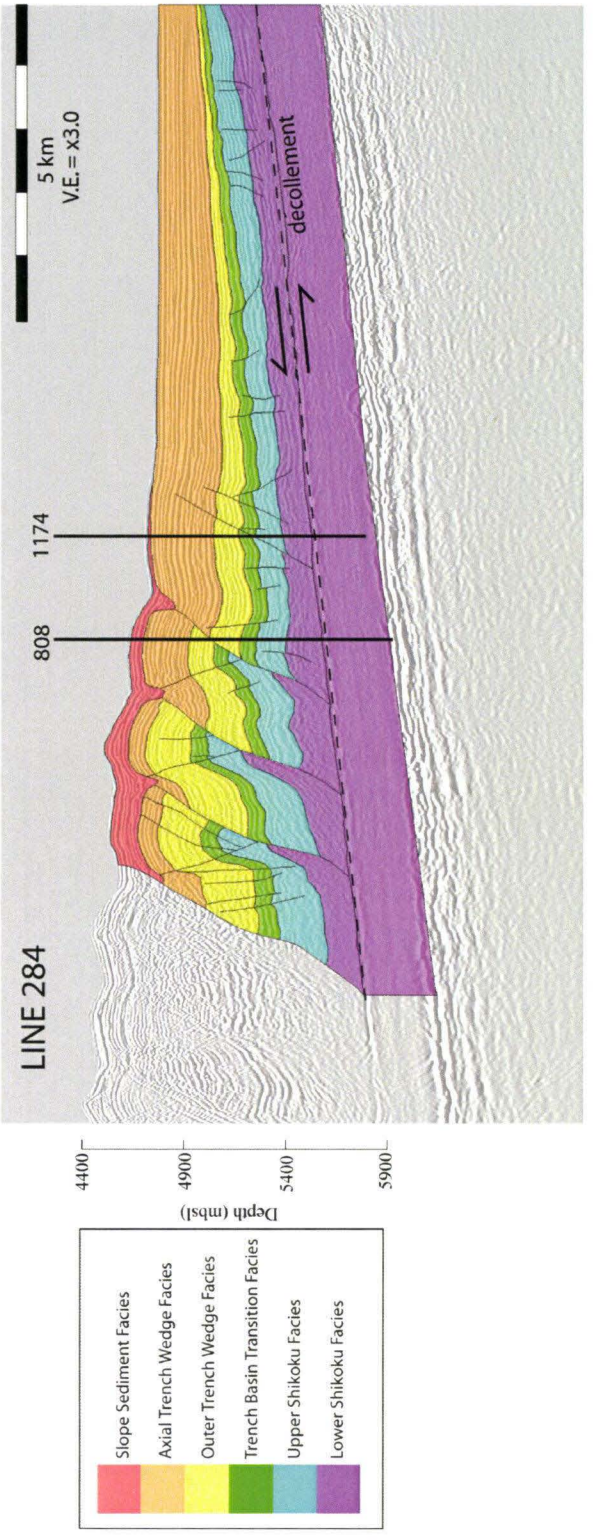
LINE 284
808
1174
5 km
V.E. = x3.0
decollement
4400
4900
5400
5900
Depth (mbsl)
Slope Sediment Facies
Axial Trench Wedge Facies
Outer Trench Wedge Facies
Trench Basin Transition Facies
Upper Shikoku Facies
Lower Shikoku Facies

Figure 4

Figure 5

Reference Location
A4
A3
A2
A1
décollement
(1)
Deformed Length
(L_f)
A4
A3
A2
A1
décollement
(2)
Restored Length (Area Balance)
(L_i)
A4 + porosity area
A3 + porosity area
A2 + porosity area
A1 + porosity area
décollement
(3)
Restored Length (Porosity Correction)
(L_i)
= total area of wedge (deformed and area balance restoration)
= total area of wedge (restored with porosity correction)
= deformed stratigraphic horizon
= restored stratigraphic horizon
Shortening Calculation:
$\frac{L_i - L_f}{L_i} \times 100\%$

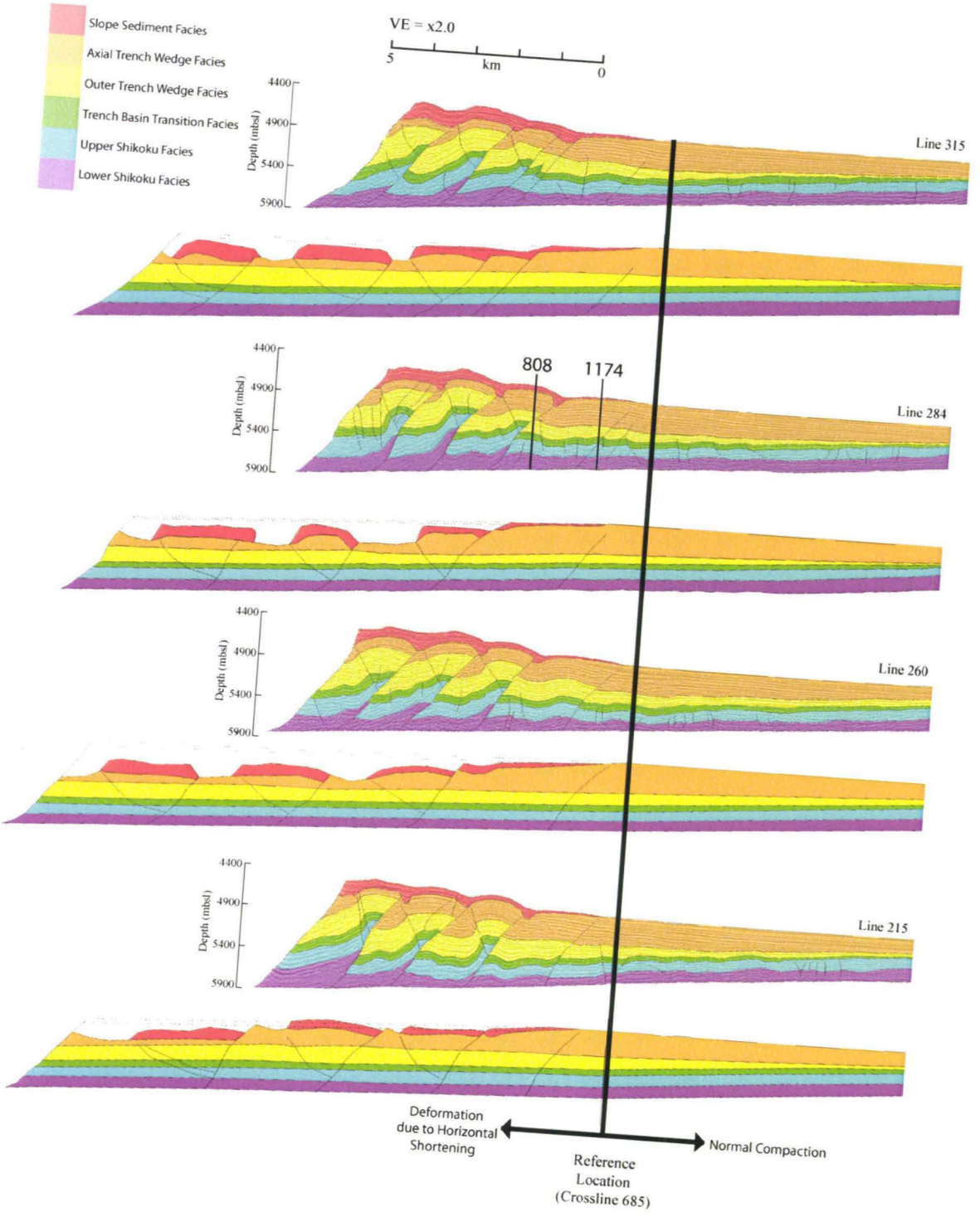
Slope Sediment Facies
Axial Trench Wedge Facies
Outer Trench Wedge Facies
Trench Basin Transition Facies
Upper Shikoku Facies
Lower Shikoku Facies
VE = x2.0
5
km
0
Depth (mbsl)
4400
4900
5400
5900
Line 315
808
1174
Line 284
Line 260
Line 215
Deformation due to Horizontal Shortening
Reference Location (Crossline 685)
Normal Compaction

Figure 6

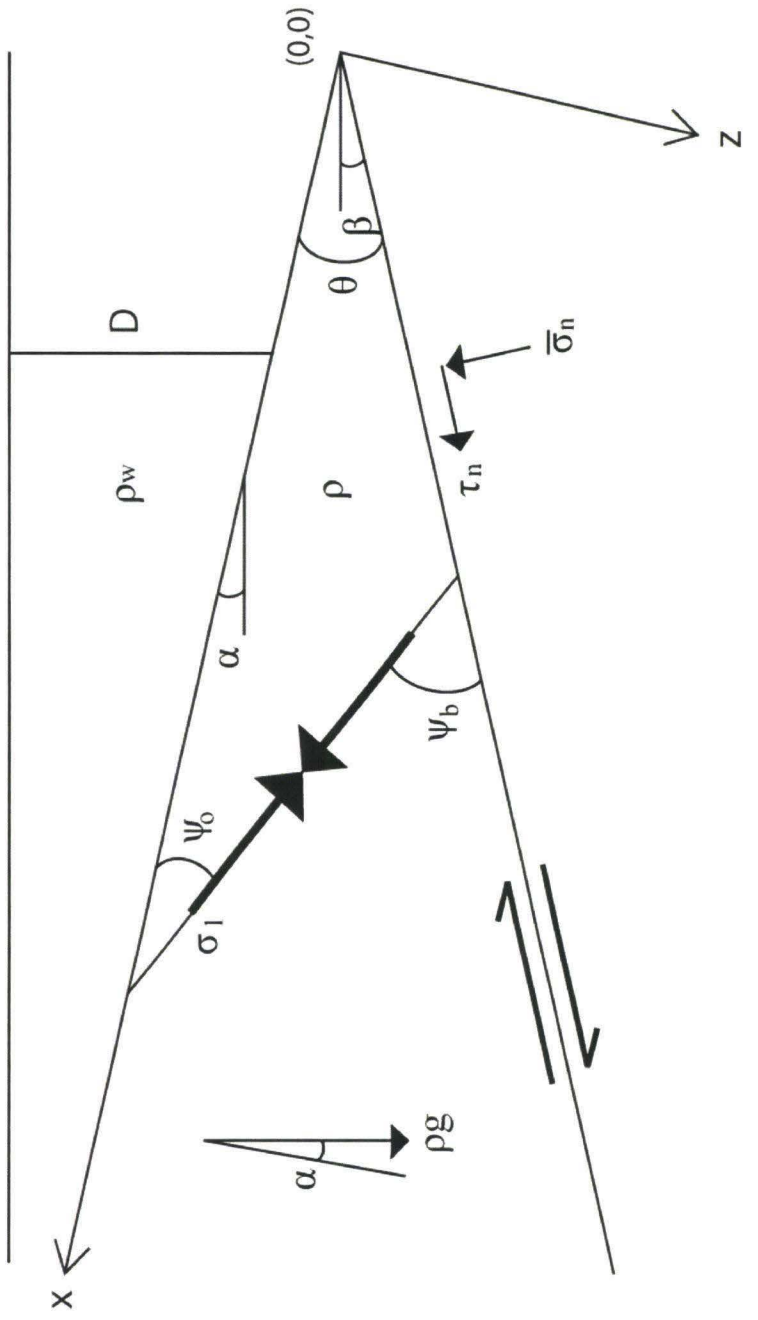

Figure 7

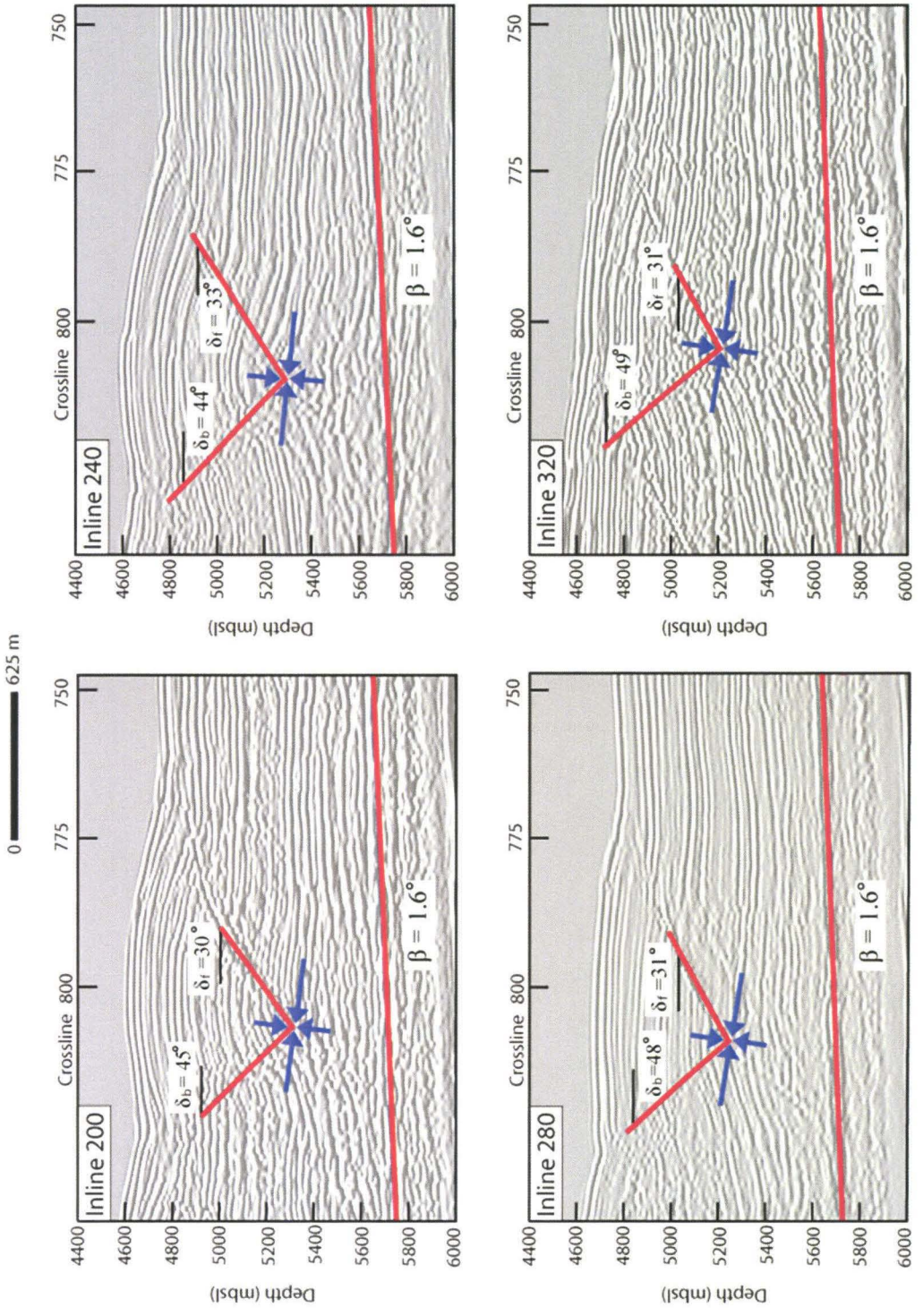
0
625 m
Inline 200
Crossline 800
775
750
Depth (mbsl)
4400
4600
4800
5000
5200
5400
5600
5800
6000
δb = 45°
δf = 30°
β = 1.6°
Inline 240
δb = 44°
δf = 33°
β = 1.6°
Inline 280
δb = 48°
δf = 31°
β = 1.6°
Inline 320
δb = 49°
δf = 31°
β = 1.6°

Figure 8

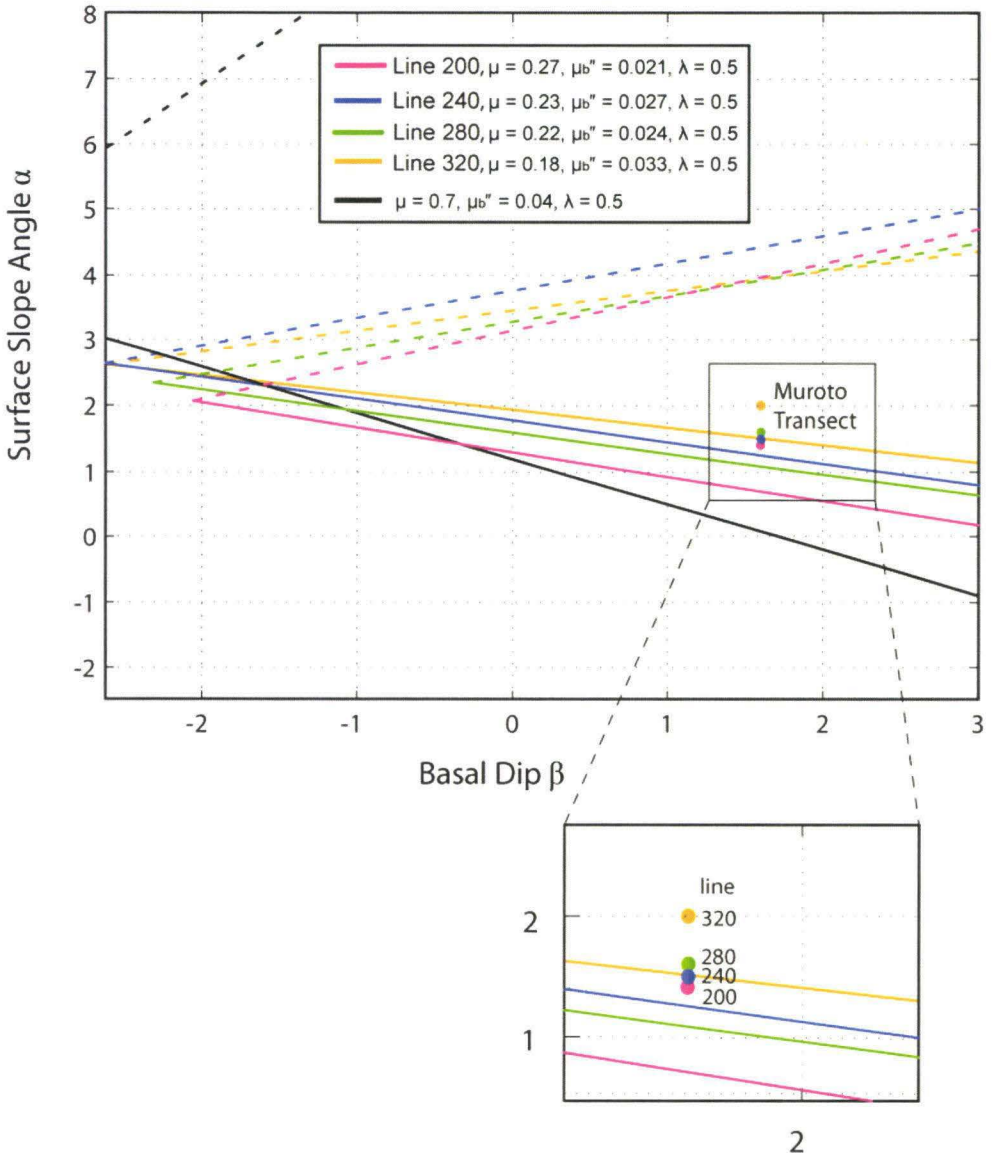
Line 200, μ = 0.27, μb″ = 0.021, λ = 0.5
Line 240, μ = 0.23, μb″ = 0.027, λ = 0.5
Line 280, μ = 0.22, μb″ = 0.024, λ = 0.5
Line 320, μ = 0.18, μb″ = 0.033, λ = 0.5
μ = 0.7, μb″ = 0.04, λ = 0.5
Muroto Transect
Surface Slope Angle α
Basal Dip β
line
320
280
240
200

Figure 9

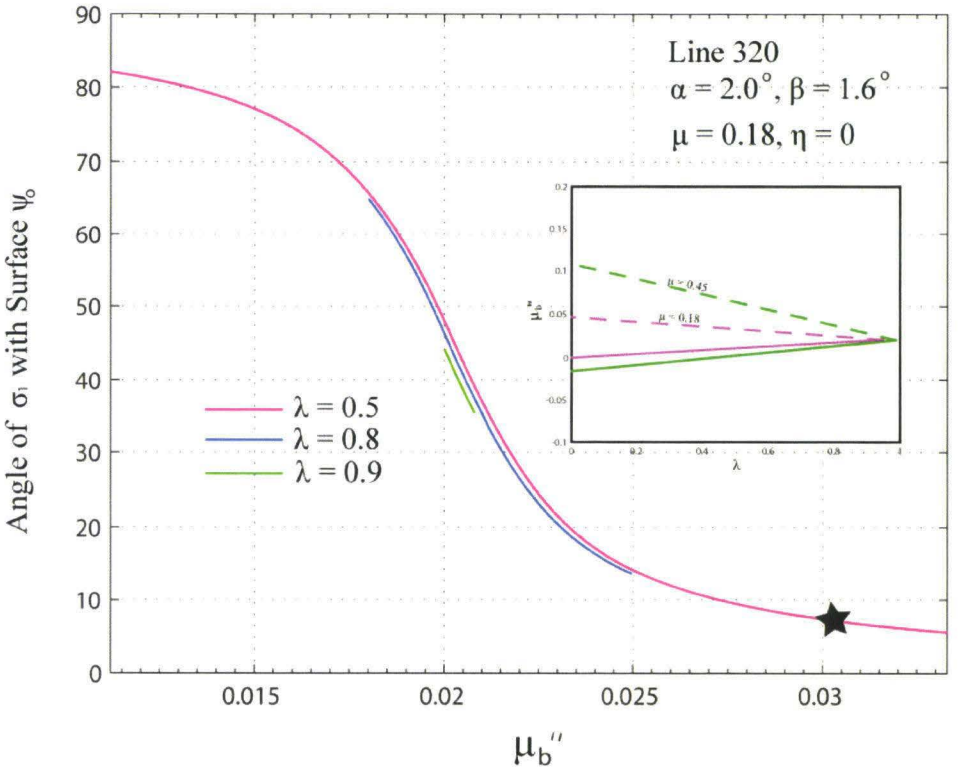
Line 320
α = 2.0°, β = 1.6°
μ = 0.18, η = 0
λ = 0.5
λ = 0.8
λ = 0.9
Angle of σ1 with Surface ψo
μb''

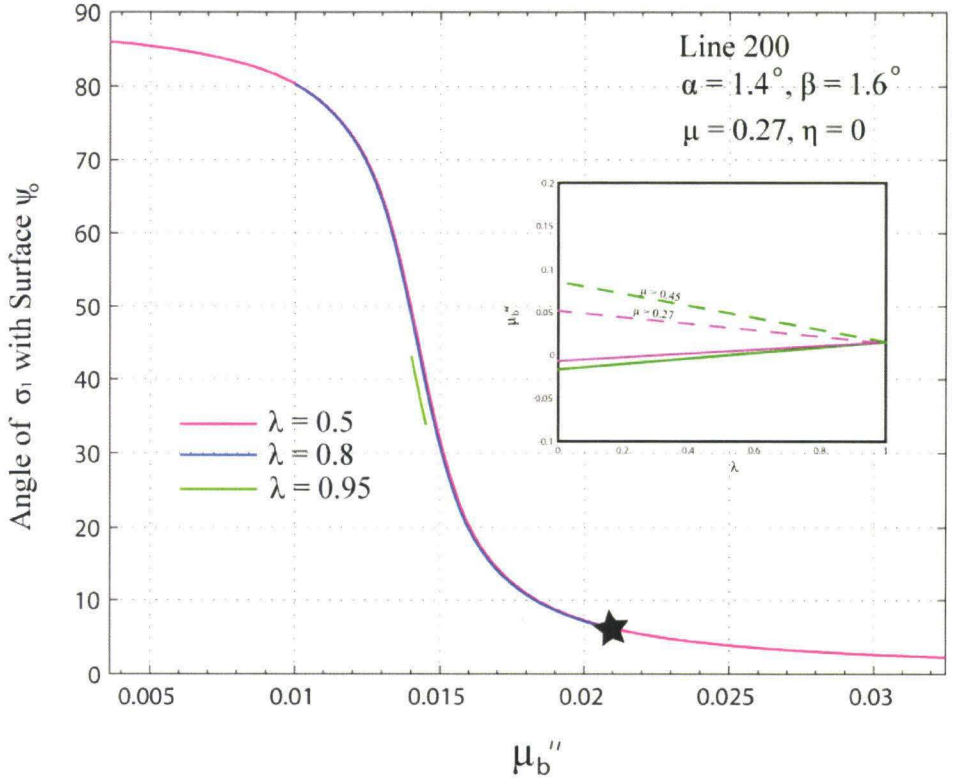
Line 200
α = 1.4°, β = 1.6°
μ = 0.27, η = 0
λ = 0.5
λ = 0.8
λ = 0.95
Angle of σ1 with Surface ψo
μb''

Figure 10

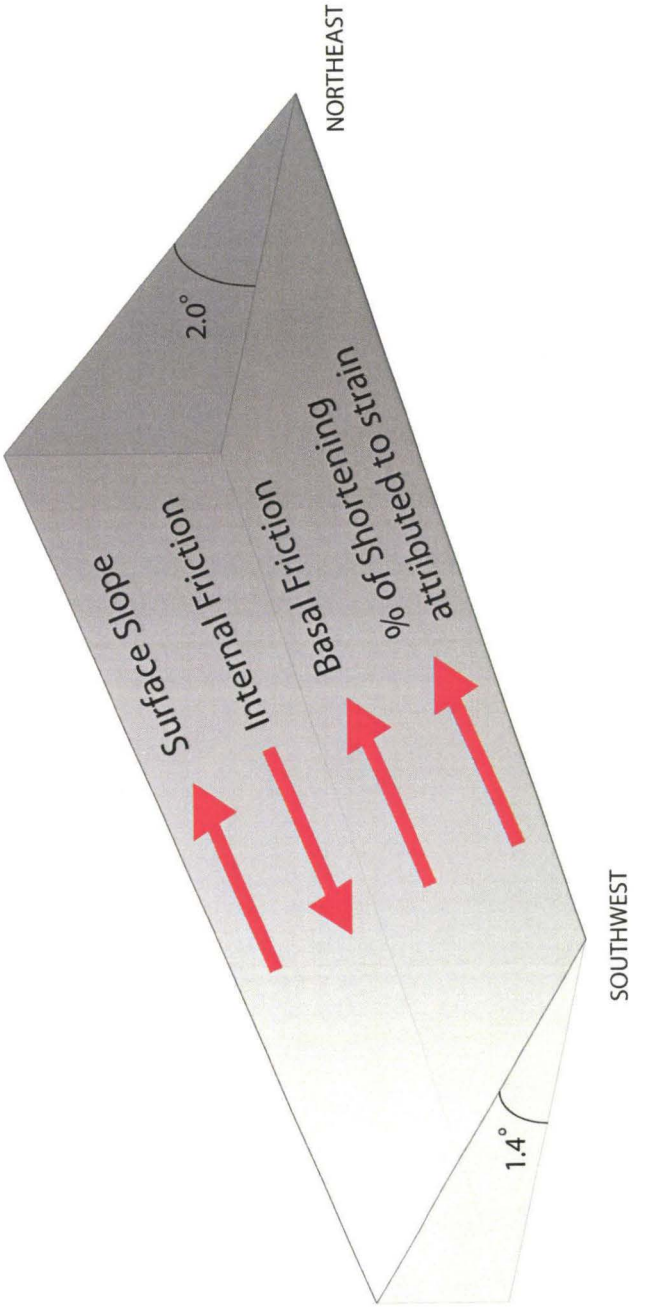
NORTHEAST
2.0°
Surface Slope
Internal Friction
Basal Friction
% of Shortening
attributed to strain
SOUTHWEST
1.4°

Figure 11

APPENDIX C: Porosity Gradients

Porosity Gradient Captions

1. Line 215
2. Line 260
3. Line 284
4. Line 315

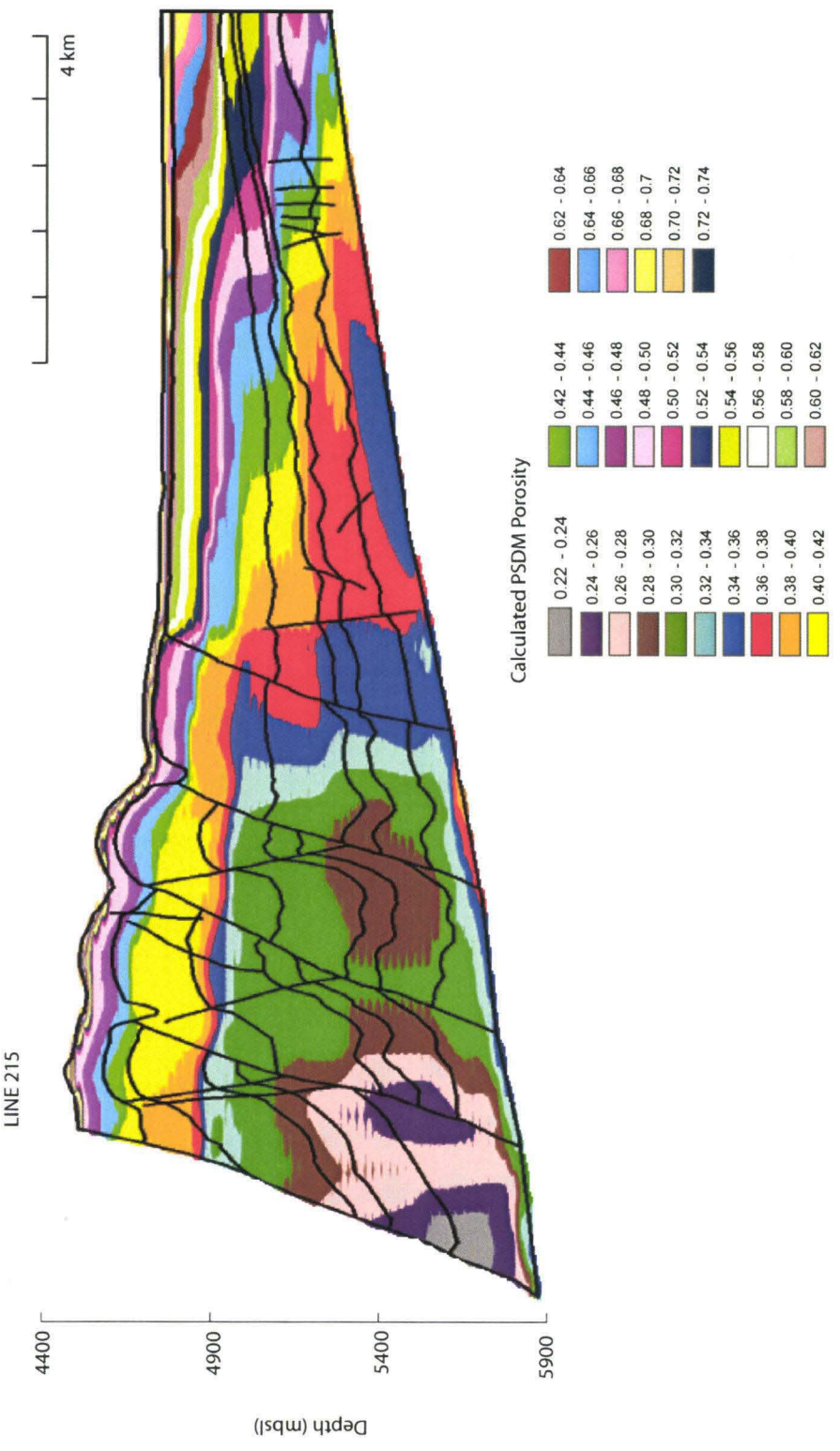
4 km
LINE 215
Depth (mbsl)
4400
4900
5400
5900
Calculated PSDM Porosity
0.22 - 0.24
0.24 - 0.26
0.26 - 0.28
0.28 - 0.30
0.30 - 0.32
0.32 - 0.34
0.34 - 0.36
0.36 - 0.38
0.38 - 0.40
0.40 - 0.42
0.42 - 0.44
0.44 - 0.46
0.46 - 0.48
0.48 - 0.50
0.50 - 0.52
0.52 - 0.54
0.54 - 0.56
0.56 - 0.58
0.58 - 0.60
0.60 - 0.62
0.62 - 0.64
0.64 - 0.66
0.66 - 0.68
0.68 - 0.7
0.70 - 0.72
0.72 - 0.74

Gradient 1

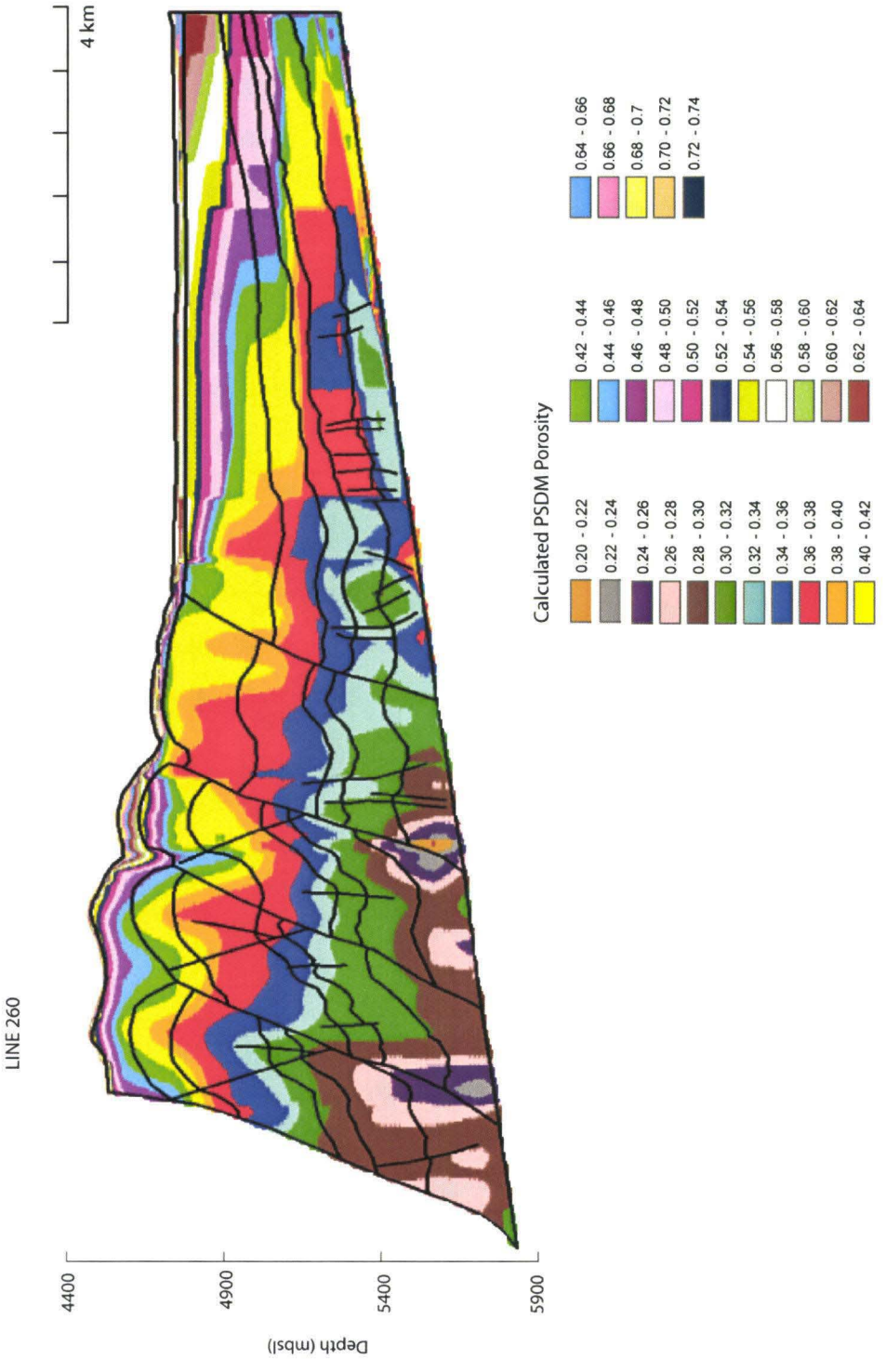
4 km
LINE 260
4400
4900
5400
5900
Depth (mbsl)
Calculated PSDM Porosity
0.20 - 0.22
0.22 - 0.24
0.24 - 0.26
0.26 - 0.28
0.28 - 0.30
0.30 - 0.32
0.32 - 0.34
0.34 - 0.36
0.36 - 0.38
0.38 - 0.40
0.40 - 0.42
0.42 - 0.44
0.44 - 0.46
0.46 - 0.48
0.48 - 0.50
0.50 - 0.52
0.52 - 0.54
0.54 - 0.56
0.56 - 0.58
0.58 - 0.60
0.60 - 0.62
0.62 - 0.64
0.64 - 0.66
0.66 - 0.68
0.68 - 0.7
0.70 - 0.72
0.72 - 0.74

Gradient 2

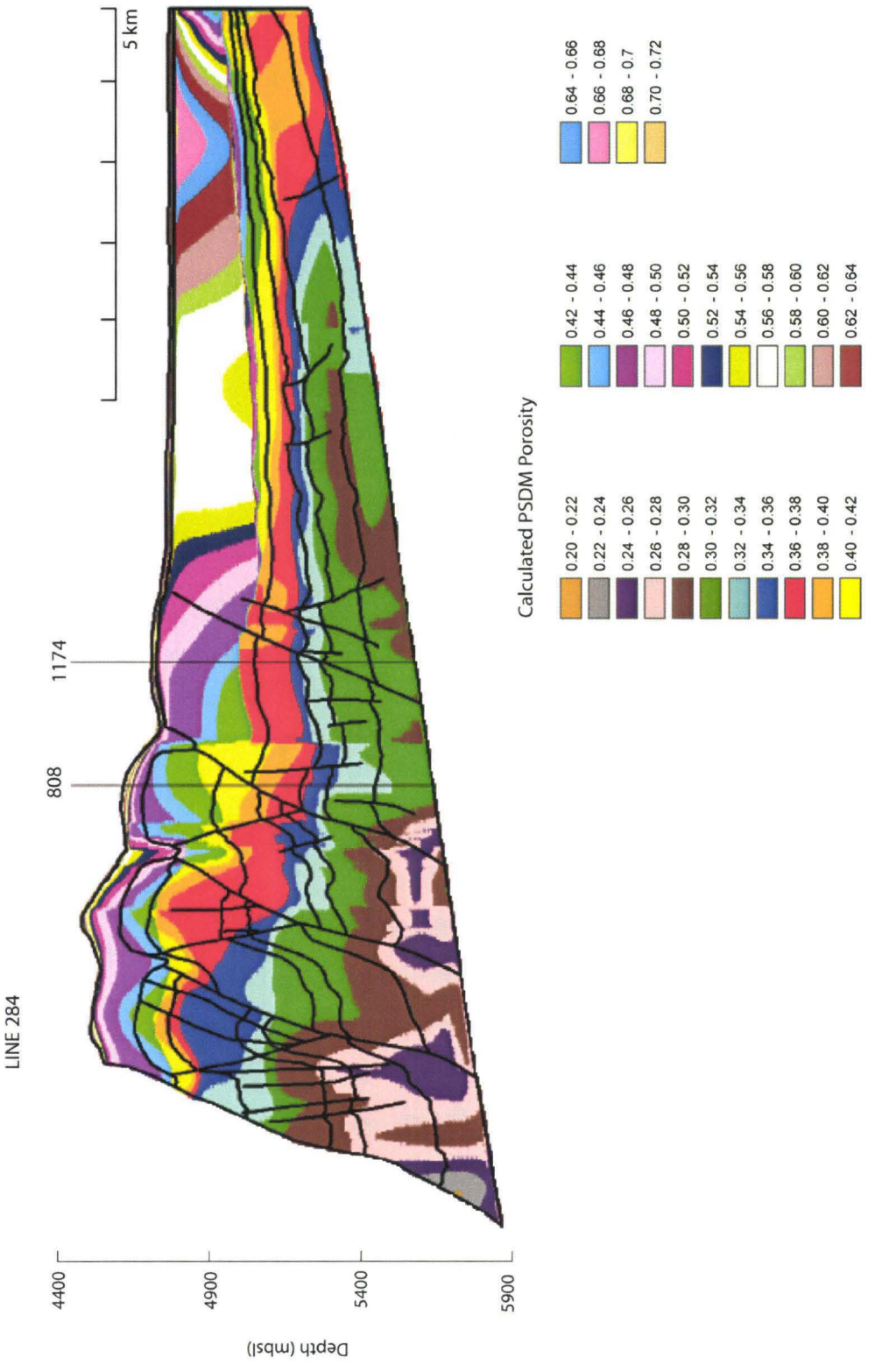
5 km
1174
808
LINE 284
4400
4900
5400
5900
Depth (mbsl)
Calculated PSDM Porosity
0.20 - 0.22
0.22 - 0.24
0.24 - 0.26
0.26 - 0.28
0.28 - 0.30
0.30 - 0.32
0.32 - 0.34
0.34 - 0.36
0.36 - 0.38
0.38 - 0.40
0.40 - 0.42
0.42 - 0.44
0.44 - 0.46
0.46 - 0.48
0.48 - 0.50
0.50 - 0.52
0.52 - 0.54
0.54 - 0.56
0.56 - 0.58
0.58 - 0.60
0.60 - 0.62
0.62 - 0.64
0.64 - 0.66
0.66 - 0.68
0.68 - 0.7
0.70 - 0.72

Gradient 3

Gradient 4

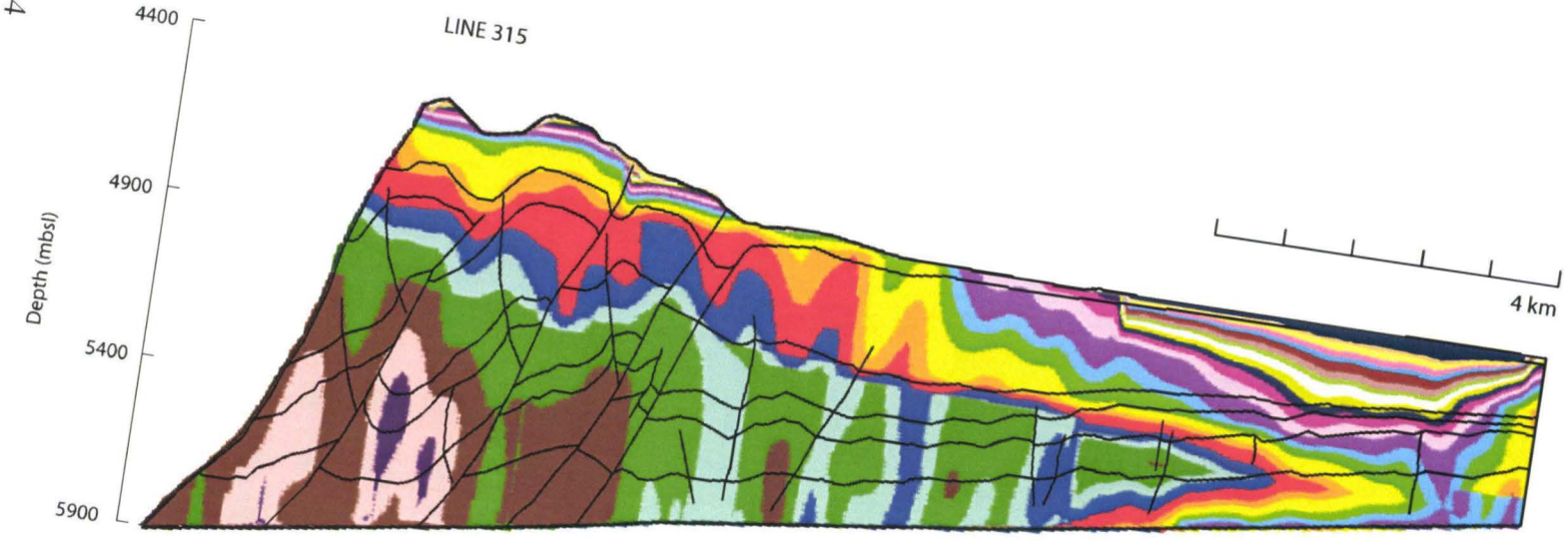

Calculated PSDM Porosity

0.24 - 0.26
0.26 - 0.28
0.28 - 0.30
0.30 - 0.32
0.32 - 0.34
0.34 - 0.36
0.36 - 0.38
0.38 - 0.40
0.40 - 0.42
0.42 - 0.44
0.44 - 0.46
0.46 - 0.48
0.48 - 0.50
0.50 - 0.52
0.52 - 0.54
0.54 - 0.56
0.56 - 0.58
0.58 - 0.60
0.60 - 0.62
0.62 - 0.64
0.64 - 0.66
0.66 - 0.68
0.68 - 0.7
0.70 - 0.72
0.72 - 0.74

APPENDIX D: Codes

Code Captions

Code 1:

Compressive and Critical Curves for a wedge of given properties

Code 2:

Elastic stress paths for a wedge of given properties

```
%Code 1

% Plots the critical curves for a wedge of given properties.
% Based on Dahlen (1984), and Xiao et al., (1991)
% Last Modified by Melody Studer, June 12, 2006.

%Inputs:
%pw, p, lambda, lambdab, phi or mu, phib or mub

%Outputs
%Yields critical taper curves of the given noncohesive wedge

pw = 1030;                  %kg/m^3
p = 2500;                   %kg/m^3
lambda = 0.65;              %Dimensionless

%Coefficient of internal friction (mu)
%Angle of internal friction (i.e., angle of repose); (phi)
%phi = deg2rad(30);
%mu = tan(phi);
mu = 0.45;
phi = atan(mu);

%Coefficient of basal friction (mub)
%Angle of internal friction; (phib)
%phib = deg2rad(10);
%mub = tan(phib);


%Relationships between friction coefficients
%mub_double_prime = (1-lambdab)*mub;
mub_double_prime = 0.04;
%mub_prime = mub*((1-lambdab)/(1-lambda));
mub_prime = mub_double_prime/(1-lambda);
phib_prime = atan(mub_prime);

mub = mub_prime;
phib = atan(mub);

%Maximum possible surface slope, independent of basal conditions
alpha_max_rad = atan((mu*(1-lambda))/(1-(pw/p)));
alpha_max_deg = rad2deg(alpha_max_rad);

%Array of alpha's given to create plots, varying between +_ alpha_max
alpha = deg2rad([-alpha_max_deg:.001:alpha_max_deg]);
```

```
%Modified slope angle, used by Dahlen (1984)
alpha_prime = atan(((1-(pw/p))/(1-lambda)).*tan(alpha));


%Psi_0 is the stress orientation angle measured between the surface slope
%and the most compressive principal stress direction
Psi_02a = (1/2)*asin(sin(alpha_prime)/sin(phi))-(1/2)*alpha_prime;


%Psi_b is the stress orientation angle measured between the basal
%decollement and the least compressive (most tensile) principal stress
%direction
Psi_b2a = (1/2)*asin((sin(phib_prime)/sin(phi)))-(1/2)*phib_prime;
Psi_b2a_deg = rad2deg(Psi_b2a);


%Theoretical Basal Dip is determined from the relationship of the stress
%orientation angles and alpha
beta2a = Psi_b2a-Psi_02a-alpha;
beta2a_deg = rad2deg(beta2a);

%%%%%%%%%%%%%%%%%%%%%%%%%%%%%%%%%%%%%%%%%%%

%Curves of the critical wedge
%The two blue curves are the critical compressional curves.  Meaning, that
%these curves define the compressional critical bounday.
%The two red curves are the critical extensional curves.  Meaning, that
%these curves define the extensional critical boundary.

%LOWER COMPRESSIVE LINE
plot((rad2deg(beta2a)),(rad2deg(alpha)), 'b')
axis([-4 15 -6 15])
%axis([-2.625 3 -2.5 8])
grid on
hold on

%UPPER COMPRESSIVE LINE
Psi_bc =(pi/2)-(1/2)*asin((sin(phib_prime)/sin(phi)))-(1/2)*phib_prime;
Psi_02c = (1/2)*asin(sin(alpha_prime)/sin(phi))-(1/2)*alpha_prime;
beta2b = Psi_bc-Psi_02c-alpha;
beta2b_deg = rad2deg(beta2b);
plot((rad2deg(beta2b)),(rad2deg(alpha)), 'b')
```

```
%UPPER EXTENSIONAL CURVE
 Psi_02d = (pi/2)-(1/2)*asin(sin(alpha_prime)/sin(phi))-(1/2)*...
    alpha_prime;
 Psi_b2d = (pi/2)-(1/2)*asin((sin(phib_prime)/sin(phi)))-(1/2)*...
    phib_prime;
 beta2d = Psi_b2d-Psi_02d-alpha;
 beta2d_deg = rad2deg(beta2d);
 plot((rad2deg(beta2d)),(rad2deg(alpha)), 'm')

 %LOWER EXTENSIONAL CURVE

 Psi_02e = (-pi/2)-(1/2)*asin(sin(alpha_prime)/sin(phi))-(1/2)*...
    alpha_prime;
 Psi_b2e = (1/2)*asin((sin(phib_prime)/sin(phi)))-(1/2)*...
    phib_prime;
 beta2e = Psi_b2e-Psi_02e-alpha;
 beta2e_deg = rad2deg(beta2e);
 plot((rad2deg(beta2e)),(rad2deg(alpha)), 'm')

%%%%%%%%%%%%%%%%%%%%%%%%%%%%%%%%%%%%%%%%%%%%%%%

%Theoretical Wedge
alpha1 = 1.4;
beta1 =1.6;
plot(beta1, alpha1, 'g.')
```

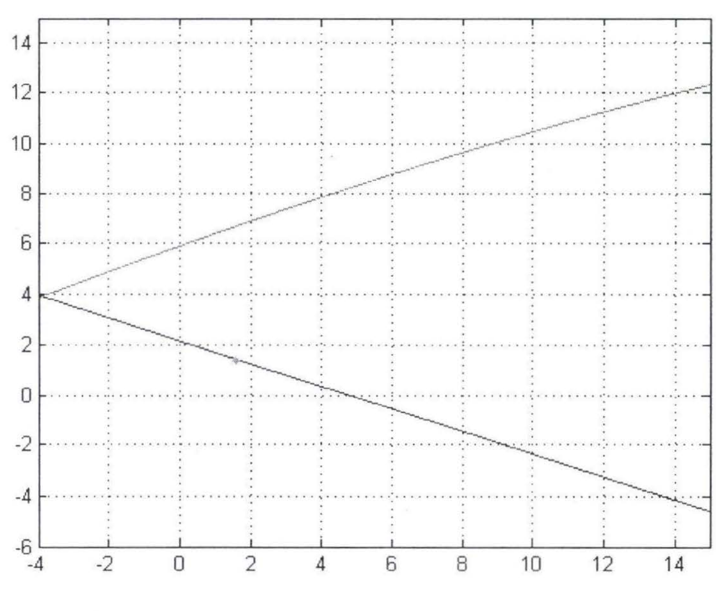

```
%Code 2

% This script shows how stresses of a given geometry change elastically
% from one state to another.

% If Psi_0e_deg is < 45, the wedge is compressively stable
% If Psi_0e_deg = 45, it is in a neutral state.
% If Psi_0e_deg > 45, the wedge is extensionally stable

%To determine the mub_double_prime value for the neutral state, use the
%value given in mub_dp_neutral_rad.

%The critical values can be found by using the critical_curves script.

%The angle Psi_o between sigma_1 and the upper surface in a stable wedge
%must be uniform.  Therefore, for a given geometry, and parameters, the
%angle Psi_0 does not change.

%Given geometry of wedge
alpha = deg2rad(2);
beta = deg2rad(1.6);
theta = alpha+beta;

%Parameters
pw = 1030;                    %kg/m^3
p = 2500;                     %kg/m^3
lambda = 0.5;                 %Dimensionless
lambdab = 0.5;                %Dimensionless
k = 0;                        %Cohesion gradient, (So/m)
g = 9.8;

mu = 0.18;
phi = atan(mu);
phi_deg = rad2deg(phi);
mub_doubleprime_basal_erosion = mu*(1-lambda)

%Mub_double_prime values need to be the two critical values
mub_double_prime = [-.05:.0001:mub_doubleprime_basal_erosion];
%mub_double_prime = 0.1;

mub_prime = mub_double_prime./(1-lambda);
phib_prime = atan(mub_prime);

mub = mub_prime./((1-lambdab)/(1-lambda));
phib = atan(mub);
```

```
alpha_max_rad = atan((mu*(1-lambda))/(1-(pw/p)));
alpha_max_deg = rad2deg(alpha_max_rad);

alpha_prime = atan(((1-(pw./p)).*sin(alpha))./...
   ((k./(p.*g.*mu))+(1-lambda).*cos(alpha)));

%Mub_double_prime solution for Psi_0 = 45 degrees
mub_dp_neutral_rad = ((1-lambda)*cos(2*theta))/(cot(alpha_prime)+...
   sin(2*theta))

%ANGLE BETWEEN THE SURFACE SLOPE AND THE PRINCIPAL
ANGLE, SIGMA1
Psi_0c= (1/2)*asin(sin(alpha_prime)/sin(phi))-(1/2)*alpha_prime;
Psi_0c_deg = rad2deg(Psi_0c);


%%%%%%%%%%%%%%%%%%%%%%%%%%%%%%%%%%%%%%%%%%%%%%%%%%%%
%ELASTIC EQUIVALENCE

A = 2.*(tan(alpha_prime)+mub_prime);
B = (sin(2*theta))*(1-mub_prime.*tan(theta));
C = (2.*tan(alpha_prime));
D = tan(theta);

m = 1+ (A./B)-(C/D);

%Cohesion gradient, defiend by k, above
n = k/((1-lambda)*mu*p*g*cos(alpha));

%Psuedoparameters
E = (m-1).^2+(4.*tan(alpha_prime).*tan(alpha_prime));
F = (2.*n+m+1).^2;

phi_p = asin(sqrt(E./F));
phi_p_deg = rad2deg(phi_p);

%Elastic Psi_0 angles
G = m - 1 + 2*(1+n);
H = m.*(csc(phi_p))-csc(phi_p);
I = asec(G./H);

Psi_0e = (1/2).*I;
Psi_0e_deg = rad2deg(Psi_0e);
```

```
% The change of Psi_0 with respect to a change in basal friction is
% referred to as the elastic stress path (Wang and Hu, 2006)

%For each geometry, Psi_0 changes between its two critical values
%corresponding to the two critical mub_double prime values

plot(mub_double_prime,real(Psi_0e_deg), 'm')
axis ([0.0112 .0333 0 90])
grid on
xlabel('u_b"')
ylabel('Angle of sigma_1 with surface Psi_0')
hold on
```

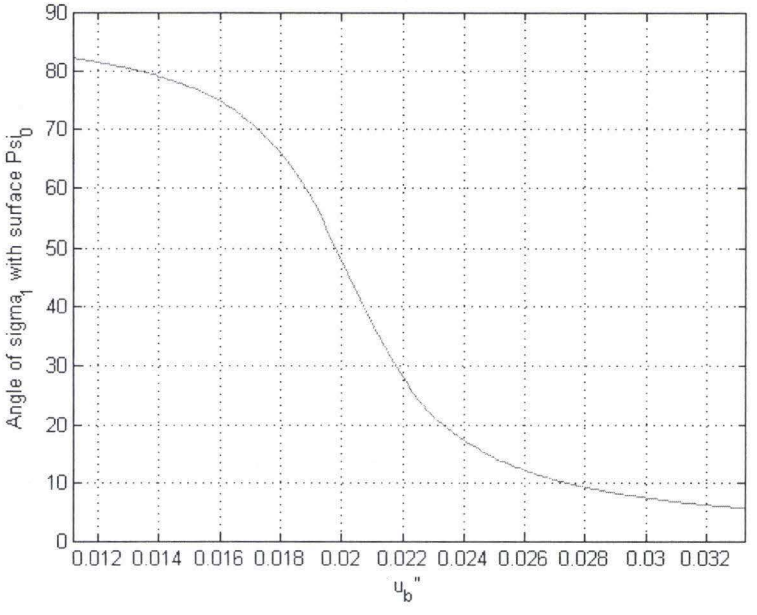

REFERENCES

Ando, M., 1975. Source mechanisms and tectonic significance of historical earthquakes along the Nankai Trough., *Japan, Tectonophysics, 27,* 119-140.

Aoki, Y., Kinoshita, H., Kagami, H., 1986. Evidence of a low-velocity layer beneath the accretionary prism of the Nankai Trough: Inference from a synthetic sonic log, *Initial Rep. Deep Sea Drill. Proj., 87,* 727-735.

Aoki, Y., Tamano, T., Kato, S., 1982. Detailed structure of the Nankai Trough from migrated seismic sections, in *Studies in Continental Margin Geology,* edited by J.S. Watkins and C.L. Drake, *AAPG Mem., 34,* 309-322.

Ashi, J., Tokuyama, H., Yamamoto, F., Uyeki, T., Tukioka, H., Taira, A., 1989. Detailed surface features of the Nankai accretionary prism obtained by IZANAGI ocean floor imaging sonar system, *Program Abstr. Seismol. Soc. Jpn., 2,* 305.

Balance, P.F., Scholl, D.W., Vallier, T.L., Stevenson, A.J., Ryan, H., Herzer, R.H., 1989. Subduction of a Late Cretaceous Seamount of the Louisville Ridge at the Tonga Trench: A Model of Normal and Accelerated Tectonic Erosion. *Tectonics*. v. 8, p. 953-962.

Bally, A. W., P. L. Gordy, and G. A. Stewart, 1966, Structure, seismic data, and orogenic evolution of southern Canadian Rocky Mountains: *Bulletin of Canadian Petroleum Geology*, v. 14, p. 337-381.

Bangs, N.L., et al., 1999. U.S.-Japan Collaborative 3-D seismic investigation of the Nankai Trough plate-boundary interface and shallow-most seismogenic zone, *Eos Trans. AGU, 80*(46), Fall Meet. Suppl., F569.

Brace, W.F., Kohlstedt, D.L., 1980. Limits on lithospheric stress imposed by laboratory experiments, *J. Geophys. Res.,* 85, 6248-6252.

Bray, C.J., and Karig, D.E., 1985. Physical properties of sediments from the Nankai Trough, Deep Sea Drilling Project Leg 87A, Sites 582 and 583. *Initial Reports, DSDP* (edited by Kagami, H., Karig, D.E., Coulobourn, W.T., *et al.*). (U.S. Govt. Printing Office) Washington, 87, 827-842.

Chapple, W.M., 1978. Mechanics of thin-skinned fold-and thrust belts. *Geological Society of America Bulletin*, 89:1189-1198.

Costa Pisani, P., Reshef, M., Moore, G.F., 2005. Targeted 3-D prestack depth imaging at Legs 190-196 ODP drill sites (Nankai Trough, Japan), *Geophysical Research Letters,* vol. 32, L20309, doi:10.1029/005GL024191.

Dahlen, F.A., Suppe, J., Davis, D., 1984. Mechanics of Fold-and-Thrust Belts and accretionary wedges: Cohesive Coulomb theory, *J. Geophys. Res.*, 89:10087-10101.

Dahlen, F.A., 1990. Critical Taper Model of Fold-and-Thrust Belts and Accretionary Wedges. *Annu. Rev. Earth Planet Sci.*, 18:55-99.

Dahlen, F.A., 1984. Noncohesive critical Coulomb wedges: An exact solution. *J. Geophys. Res.,* 89:10125-10133.

Dalhstrom, C.D.A., 1969. Balanced cross-sections: *Canadian Journal of Earth Sciences,* v. 6, p. 743-757.

Davis, D., Suppe, J., Dahlen, F.A., 1983. Mechanics of Fold-and-Thrust Belts and Accretionary Wedges, *J. Geophys. Res.,* 88:1153-1172.

Davis, D..M., Engelder, T., 1985. The role of salt in fold-and-thrust belts, *Tectonophysics,* 119, 67-88.

Davis, D.M., and von Huene, R., 1987. Inferences on sediment strength and fault friction from structures at the Aleutian trench, *Geology, 15,* 517-522.

Davis, E., Becker, K., Wang, K., Obara, K., and Ito, Y., 2006. A discrete episode of seismic and aseismic deformation of the Nankai subduction zone accretionary prism and incoming Philippine Sea plate, *Earth Planet. Sci. Lett., 242,* 73-84.

Davison, I., 1986, Listric normal fault profiles: calculation using bed-length balance and fault displacement: *Journal of Structural Geology*, v. 8, p. 209-210.

Emerman, S., Turcotte, D., 1983. A fluid model for the shape of accretionary wedges, *Earth Planet. Sci. Lett.,* 63, 379-384.

Erickson, S.N., and Jarrard, R.D., 1998. Velocity-porosity relationships for water-saturated siliciclastic sediments. *J. Geophys. Res.,* 103:30385-30406.

Feeser, V., Moran, K., Bruckmann, W., 1993. Stress-regime controlled yield and strength behavior of sediment from the frontal part of the Nankai accretionary prism, *Proc. Ocean Drill. Program Sci. Results, 131,* 261-274.

Goff, D., and Wiltschko, D.V., 1992. Stresses beneath a ramping thrust sheet. *J. Struct. Geol.* 14, 437-449.

Gulick, S.P.S, Bangs, N.L.B., Shipley, T.H., Nakamura, Y., Moore, G., Kuramoto, S., 2004. Three-dimensional architecture of the Nankai accretionary prism's imbricate thrust zone off Cape Muroto, Japan: Prism reconstruction via en

echelon thrust propagation, *J. Geophys. Res.,* 109: B02105, doi:10.1029/2003JB002654.

Gutscher, M.A., Growth, erosion and material transfer in accretionary wedges: A qualitative analysis based on analog modeling and the implications for the evolution of convergent margins, Ph.D. thesis, Univ. Kiel, Kiel, Germany, 1996.

Hoshino, K., Koide,H., Inami, K., Iwamura, S., Mitsui, S., 1972. Mechanical properties of Japanese Tertiary sedimentary rocks under high confining pressure, *Rep.* 244, 200 pp., Geol. Surv. of Jpn., Kawasaki.

Hu, Y., Wang, K., 2006. Bending-like behavior of thin wedge-shaped elastic fault blocks. *J. Geophys. Res.,* 111, No. B6, BO6409, doi:10.1029/2005JB003987.

Ito, Y., Obara, K., 2006. Dynamic deformation of the accretionary prism excites very low frequency earthquakes, *Geophys. Res. Lett., 33,* L02311, doi:10.1029/2005GL025270.

Kaiko I Research Group, 1986. Topography and Structure of Trenches around Japan – Data Atlas of Franco-Japanese Kaiko Project, Phase I, Univ. of Tokyo Press, Tokyo.

Karig. D.E., and Angevine, C.L., 1985. Geologic constraints on subduction rates in the Nankai Trough. *Initial Reports, DSDP* (edited by Kagami, H., Karig, D.E., Coulbourn, W.T., *et al.*). (U.S Govt. Printing Office) Washington, 87, 789-796.

Kodaira, S., Takahashi, N., Park, J., Mochizuki, K., Shinohara, M., Kimura, S., 2000. Western Nankai Trough seismogenic zone: Results from a wide-angle ocean bottom seismic survey, *J. Geophys. Res., 105,* 5887-5905.

Kopp, H., and Kukowski, N., 2003. Backstop geometry and accretionary mechanics of the Sunda margin, *Tectonics, 22(6),* 1072, doi:10.1029/2002TC001420.

Kukowski, N., Schollhorn, T., Huhn, U., von Rad, S., Husen, S., and Flueh, E., 2001. Morphotectonics and mechanics of the central Makran accretionary wedge off Pakistan, *Mar. Geol., 173,*1-19.

Kuramoto, S., et al., 2001. Surface observations of subduction related mud volcanoes and large thrust sheets in the Nankai subduction margin: Report on YK00-10 and YK01-04 cruises, *JAMSTEC J. Deep Sea Res., 19,* 131-139.

Lallemand, S.E., Schnurle, P., and Malavielle, J., 1994. Coulomb theory applied to accretionary and nonaccretionary wedges: Possible causes for tectonic erosion and/or frontal accretion, *J. Geophys. Res.,* 99, 12,033-12,055.

Leggett, J., Aoki, Y., Takefumi, T., 1985. Transition from frontal accretion to underplating in a part of the Nankai Trough Accretionary Complex off Shikoku (SW Japan) and extensional features on the lower trench slope, *Mar. Pet. Geol., 2,* 131-141.

LePichon, X., et al., 1987a. Nankai Trough and fossil Shikoku Ridge results of Box 6 Kaiko survey, *Earth Planet Sci. Lett., 83,* 186-198.

LePichon, X., et al., 1987b. Nankai Trough and Zenisu Ridge: A deep-sea submersible survey, *Earth Planet Sci. Lett., 83,* 285-299.

Mikada, H., et al., 2002. *Proceedings of the Ocean Drilling Program, Initial Reports*[CD-ROM], vol. 196, Ocean Drill. Program, College Station, Tex.

Mikada, H., et al., 2003. Hydrologeological and geothermal studies around Nankai Trough (KR02-10 Nankai Trough cruise report), *JAMSTEC J. Deep Sea Res., 22,* 125-171.

Moore, G.F., Shipley, T.H., Stoffa, P.L., Karig, D.E., Taira, A., Kuramoto, S., Tokuyama, H., Suyehiro, K., 1990. Structure of the Nankai Trough Accretionary Zone from Multichannel Seismic Relfection Data, *J. Geophys. Res.*, 95:8753-8765.

Moore, G.F., Shipley, T.H., 1993. Character of the décollement in the Leg 131 area, Nankai Trough, *Proc. Ocean Drill. Program Sci. Results, 131,* 73-82.

Moore, G.F., Karig, D.E., Shipley, T.H., Taira, A., Stoffa, P.L., Wood, W.T., 1991. Structural framework of the ODP Leg 131 area, Nankai Trough, *Proc. Ocean Drill. Program Initial Rep., 131,* 15-20.

Moore, G.F., et al., 2001a. Data report: Structural setting of the Leg 190 Muroto transect, data report, *Proc. Ocean Drill. Program Initial Rep.*[CD-ROM], *131,* 1-14.

Moore, G.F., et al., 2001b. *Proc. Ocean Drill. Program Initial Rep.*[CD-ROM], vol. 190, Ocean Drill. Program, College Station Tex

Moore, G.F., et al., 2001c. New insights into deformation and fluid flow processes in the Nankai Trough accretionary prism: Results of Ocean Drilling Program Leg 190, *Geochem. Geophys.,* 2, paper number 2001GC000166.

Moore, J.C., Klaus, A., Bangs, N.L., Bekins, B., Bucker, C.J., Bruckmann, W., Erickson, S.N., Hansen, O., Horton, T., Ireland, P., Major, C.O., Moore, G.F., Peacock, S., Saito, S., Screaton, E.J., Shimeld, J.W., Stauffer, P.H., Taymaz, T., Teas, P.A., Tokunaga, T., 1998. Consolidation patterns during intiation and

evolution of a plateboundary décollement zone: Northern Barbados Accretionary Prism, *Geology, 26:*811-814.

Morgan, J.K., and Karig, D.E., 1995. Kinematics and a balanced and restored cross-section across the toe of the eastern Nankai accretionary prism, *J. of Structural Geology,* 17:31-45.

Nasu, N., et al., 1982. Mulitchannel seismic reflection data across Nankai Trough, report, Ocean Red. Inst, Univ. of Tokyo, Tokyo.

Ohmori, K., Taira, A., Tokuyama, H., Sagaguchu, A., Okamura, M, Aihara, A., 1997. Paleothermal structure of the Shimanto accretionary prism, Shikoku, Japan: Role of an out-of-sequence thrust, *Geology, 5,* 325-330.

Park, J.O., Tsuru, T., Kaneda, Y., Kono, Y., Kodiara, S., Takahasi, N., Kinoshita, H., 1999. A subducting seamount beneath the Nankai accretionary prism off Shikoku, southwestern Japan, *Geophys. Res. Lett., 26,* 931-934.

Park J.O., Tsuru, T., Kodiara, S., Nakanisi, A., Miura, S., Kaneda, Y., Kono, Y., 2000. Out-of-sequence thrust faults developed in the coseismic slip zone of the 1946 Nankai earthquake (M_w = 8.2) off Shikoku, southwest Japan, *Geophys, Res. Lett., 27,* 1033-1036.

Saffer, D.M., and Bekins, B.A., 2002. Hydrologic controls on the morphology and mechanics of accretionary wedges, *Geology, 30,* 271-274.

Screaton, E., Saffer, D., Henry, P., Hunze, S., Leg 190 Shipboard Scientific Party, 2002. Porosity loss within the underthrust sediments of the Nankai accretionary complex: Implications for overpressures. *Geo. Soc. of America, 30,* 19-22.

Seno, T., Stein, S., Gripp, A.E., 1993. A model for the motion of the Philippine Sea Plate consistent with NUVEL-1 and geological data, *J. Geophys, Res., 98,* 17941-17948.

Shipley, T.H., McIntosh, K.D., Silver, E.A., 1992. Three-Dimensional Seismic Imaging of the Costa Rica Accretionary Prism: Structural Diversity in a Small Volume of the Lower Slope. Jour. of Geophys. Res. v. 97, p. 4439-4459.

Stockmal, G.S., 1983. Modeling of large-scale accretionary wedge deformation, *J. Geophys. Res.,* 88, 8271-8287.

Taira, A., et al., 1991. *Proceedings of the Ocean Drilling Program, Initial Reports,* vol. 131, Ocean Drill. Program, College Station, Tex.

Taira, A., 2001. Tectonic Evolution of the Japanese Island Arc System. *Ann. Rev. Earth and Planet. Sci.* 29:109-134.

Taira, A., et al., 1991. *Proceedings of the Ocean Drilling Program, Initial Reports,* vol. 131, Ocean Drill. Program, College Station, Tex.

Taira, A., Katto, J., Tashihiro, M., Okamura, M., and Kodama, K., 1988. The Shimanto Belt in Shikoku, Japan: Evolution of Cretaceous to Miocene accretionary prism, *Mod. Geol.,* 12, 5-46.

Taira, A., and Tashihiro, M., 1987. Late Paleozoic and Mesozoic accretion tectonics of Japan and eastern Asia*, in Historical Paleogeography an Plate Tectonic Evolution of Japan and Eastern Asia,* edited by A. Taira and M. Tashihiro, 1-47, Terra Publ., Tokyo.

Tamano, T., Toba, T., and Aoki, Y., 1983. Development of forearc continental margins and their potential for hydrocarbon accumulation, *Proceeding of the Worl Petrology Congress,* 1-11, Portland Press, Colchester, UK.

von Huene, R., and Klaeschen, D., 1999. Opposing gradients of permanent strain in the aseismic zone and elastic strain across the seismogenic zone of the Kodiak shelf and slope, Alaska, *Tectonics, 18,* 248-262.

Wang, K., Dixon, T., 2004. "Coupling" semantics and science in earthquake research (Forum article), *Eos Trans. AGU* 85, 180.

Wang, K., He, J., 1999. Mechanics of low-stress forearcs: Nankai and Cascadia, *J. Geophys. Res.,* 104, 15,191-15,205.

Wang, K., Hu,Y., 2006. Accretionary prisms in subduction earthquake cycles: The Theory of dynamic Coulomb wedge. *J. Geophys. Res.*, 111, No. B6, B06410, doi:10.1029/2005JB004094.

Woodward, N.B., Boyer, S.E., and Suppe, J., 1985. An outline of balanced cross-sections. U. Tenn., Dept. Geol. Sci., *Studies in Geology,* 11.

Xiao, H., and J. Suppe, 1993, Origin of rollover: *AAPG Bulletin*, v. 76, p. 509-529.

Yin, A., Kelty, T.K., 2000. An elastic wedge model for the development of coeval normal and thrust faulting in the Mauna Loa-Kilauea rift system in Hawaii. *J. Geophys. Res.,* 105:25909-25925.

Yin,A., 1993. Mechanics of Wedge-Shaped Fault Blocks, 1. An Elastic Solution for Compressional Wedges. *J. Geophys. Res.*, 98: 14245-14256.

Zhao, W.L., Davis, D.M., Dahlen, F.A., Suppe, J., 1986. Origin of Convex Accretionary Wedges: Evidence from Barbados. *J. Geophys. Res.*, 91:10,246-10,258.